Office of Naval Research

Contract N00014-78-C-0636|NR 064-610

Technical Report No. 14

Report No. GIT-CACM-SNA 12

by

T. Nishioka and S.N. Atluri

Finite Element Simulation of Fast Fracture
in Steel DCB Specimen.

July 81
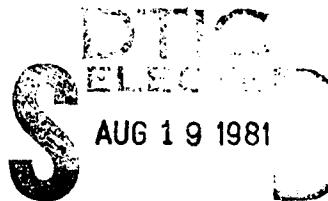
DTIC
SELECT
AUG 19 1981

A

Center for the Advancement of Computational Mechanics
School of Civil Engineering
Georgia Institute of Technology
Atlanta, Georgia 30332

81 8 18 072

FINITE ELEMENT SIMULATION OF FAST FRACTURE

IN STEEL DCB SPECIMEN

T. Nishioka* and S.N. Atluri**

Center for the Advancement of Computational Mechanics
School of Civil Engineering
Georgia Institute of Technology, Atlanta, GA   30332

*   Research Scientist II
** Regents' Professor of Mechanics

Abstract:

Results of a numerical simulation, based on an energy consistent moving singularity dynamic finite element procedure, of fast crack propagation and arrest in a high strength steel DCB specimen are presented. The influence of material properties of high strength steel on dynamic crack propagation and arrest is investigated. The influence of the loss of contact of specimen with the loading wedge is also critically examined. The present numerical results are compared with available experimental data. It is found that the present results agree well with available experimental data, and the crack arrest toughness values obtained in the present analysis correlate well with the ratio of the maximum kinetic energy of the specimen to the input energy.

Introduction:

The techinque of the measurement of dynamic stress intensity factors for fast running and arresting cracks in specimen made from a transparent photoelastic material, Aralidite B, has been developed by Kalthoff et al [1,2,3]. In the experiments, stress intensity factors for fast running cracks were measured by means of the shadow optical method of caustics. This method was later applied for a nontransparent specimen [4]. The stress intensity factors were measured by the caustics reflected from the mirrored surface of a high strength steel specimen. In the case of high strength steel, the overall variation of stress intensity factors during the crack propagation was found to be similar to that in Araldite B. For some portion of the crack propagation phase, however, the stress intensity factors in the high strength steel specimen show large oscillations, whereas the data for Araldite B specimen can be represented by a rather smooth curve. The authors in Ref. [4] attribute this oscillation to high frequency stress waves interacting with the crack. However, it is the present authors' opinion that these oscillations may be limited to the surface of the

specimen, due to the presence of vibration of the specimen surface. Therefore, stress intensity factors along the crack front within the specimen thickness may be expected to show a rather smooth variation.

The primary objective of the present paper is an attempt to simulate the crack propagation and arrest by using the data for steel specimens presented in Ref. [4]. The authors have presented a "moving singularity" finite element procedure for simulation of fast crack propagation in finite bodies [5,6,7]. This special finite element method has been previously applied, for the "generation" and "prediction" phase calculations of dynamic fracture in DCB specimen made from the model-material Araldite B [8], and for analysis of dynamic fracture in dynamic tear test specimen [9].

In Ref. [4], insufficient data for crack propagation history which are required in the present generation phase study [calculation of dynamic K-factors for a given crack-propagation history] have been measured in the experiment. In the present paper three curves for crack propagation history are hypothesized to perform the calculation. The influence of material constants on crack propagation and arrest in DCB specimen is also investigated by changing Young's modulus E, Poisson's ratio ν and the mass density ρ. In addition, in the present paper, careful attention is paid to the wedge-loading condition. Both fixed and contact/no-contact loading conditions are analyzed. The obtained numerical results are critically examined and some conclusions that may be germane to the process of crack propagation in structural steels are made.

Outline of Moving Singularity Finite Element Method:

In the procedure adopted in the paper, the basis functions used for displacement, velocity, and acceleration in the singular element near the crack-tip are:

$$u_\alpha(\xi, x_2, t) = u_{\alpha j}(\xi, x_2, b)\beta_j(t) \quad [\alpha=1,2; \ j=1,\ldots,N] \tag{1}$$

$$\dot{u}_\alpha = u_{\alpha j}\dot{\beta}_j - v u_{\alpha j,\xi}\beta_j \tag{2}$$

$$\ddot{u}_\alpha = u_{\alpha j}\ddot{\beta}_j - 2v u_{\alpha j,\xi}\dot{\beta}_j + v^2 u_{\alpha j,\xi\xi}\beta_j \tag{3}$$

where $u_{\alpha j}$ correspond to the "steady-state" (i.e., which are invariant to an observer moving with the crack-tip) eigen-function solutions for the elasto-dynamic wave equations (with independent variables ξ, and x_2) for crack propagation at constant velocity v in a plane domain. Note that $x_\alpha (\alpha=1,2)$ are fixed coordinates, with $x_2=0$ defining the crack plane and $\xi=x_1-vt$. It is noted that the first term, viz., $u_{\alpha 1}$, leads to the appropriate $(r^{-\frac{1}{2}})$ type singularity in strains and stresses. The singular element in the present procedure is surrounded by the usual isoparametric [8-noded, in the present case] elements. The displacement compatibility between the singular element and the surrounding isoparametric elements is satisfied in the present analysis through a least-square technique [5,6].

Consider two instants of time, t_1 and $t_2=t_1+\Delta t$. Assuming that in a Mode I crack propagation problem, the crack-lengths at t_1 and t_2 are, respectively, Σ_1 and $\Sigma_1+\Delta\Sigma$. Let the displacements, strains, and stresses at t_1 be denoted by u_i^1, ε_{ij}^1, and σ_{ij}^1, respectively, while those at t_2 are denoted by a superscript 2 for each variable. The variables at time t_1 are presumed to be known. It has been shown in [5,6] that the variational principles governing the dynamic crack propagation between times t_1 and t_2 can be written as:

$$\int_{V_2} (\sigma_{ij}^2+\sigma_{ij}^1)\delta\varepsilon_{ij}^2 + \rho(\ddot{u}_i^1+\ddot{u}_i^2)\delta u_i^2 \, dV$$

$$= \int_{S_{\sigma_2}} (\bar{T}_i^1+\bar{T}_i^2)\delta u_i^2 ds + \int_{\Sigma_1^+} (\bar{T}_i^2+\bar{T}_i^1)^+(\delta u_i^2)^+ ds$$

$$+ \int_{\Delta\Sigma^+} (\bar{T}_i^2+\sigma_{ij}^1 v_j^1)^+(\delta u_i^2)^+ ds \tag{4}$$

- 3 -

where V_2 is the domain of the body, and S_{σ_2} is the boundary of V_2 where tractions are prescribed, at time t_2. $\bar{T}_i^1$ are the prescribed tractions at time t_1 at S_{σ_1} ($=S_{\sigma_2}$) and $\bar{T}_i^2$ are the prescribed tractions at S_{σ_2} as well as at the newly created crack surface $\Delta\Sigma$ at time t_2. It is seen that σ_{ij}^1 v_j^1 at $\Delta\Sigma$ are the cohesive forces holding the crack-face together at time t_1. In the above, mode I conditions are assumed; hence, only the upper half of the domain with the crack face Σ^+ is considered.

In the variational principle in Eq. (4), the variables $\ddot{u}_i^1$, and σ_{ij}^1 are presumed to be known; while σ_{ij}^2, ε_{ij}^2 and u_j^2 are the variables. The variables u_j^2 are assumed according to Eq. (1), with the velocity v_2 appearing in them. Further, the variational principle in Eq. (4) is used to develop a discrete (finite element) approximation for a (finite element) mesh at time t_2. Note that at time t_2, in the present problem, the crack-tip is located at $x=\Sigma_1+\Delta\Sigma$. In developing the equations for the finite element mesh at t_2, it is seen from Eq. (4), that the variation of σ_{ij}^1 and u_j^1 must be known in the finite element mesh at time t_2. However, σ_{ij}^1 and u_j^1, and $\ddot{u}_j^1$ were solved for, in the finite element mesh at t_1. In the mesh at t_1 the crack-tip is located at $x_1=\Sigma_1$ and hence the crack-element is centered at Σ_1. Thus, between t_1 and t_2 ($=t_1+\Delta t$) the crack-element is translated by an amount $\Delta\Sigma$. While the crack-element is translated, only the elements immediately surrounding the moving crack-tip are distorted. Thus the finite meshes at times t_1 and t_2 differ only in the location of crack-tip (and hence the crack-element) and the shapes of the immediately surrounding isoparametric elements. Thus, the known data for σ_{ij}^1 and u_j^1 in the mesh at t_1 is interpolated easily into corresponding data in the mesh at t_2. Based on these concepts, the development of the finite-element equations form the principle in Eq. (4), and the numerical integration of these equations follows the well-established procedures. Further details

can be found in [5,6] where it is shown that the dynamic k-factors can be computed directly in the present analysis procedure.

Analysis Procedure for Double-Cantilever-Beam Specimen:

The test specimen geometry is indicated in Fig. 1 along with the initial configuration of the finite element mesh. Because of symmetry, only the upper half of the DCB specimen is modeled in the present analysis. Point L in Fig. 1 represents the loading point. Forty six 8-noded isoparametric elements and one moving singularity element shown by the shaded area are used. The specimen geometry indicated in Fig. 1 corresponds to that reported in Ref. [4], and a plane-stress condition is invoked in the present two-dimensional analysis.

In the present series of computations, the crack growth history is used as input data to the "generation phase" fracture simulation. As output of these generation phase computations, dynamic stress intensity factors for the propagating crack is directly obtained as a function of time. Fig. 2 shows three types of data for the crack extension history $\Sigma = \Sigma(t)$ as well as the crack velocity history $v = v(t)$, i.e., Data 1, Data 2, and Data 3. The data obtained by experiment in Ref. [4] are shown by the solid lines. To complete the input data, the broken lines are assumed, as plausible extensions of the experimentally measured datea. The crack extension histories are obtained by integrating the crack velocity histories for each case.

In Ref. [4], the crack initiation stress intensity factor for a blunt notch, K_{IQ}, was quoted as 224 MNm$^{-1.5}$. Prior to the dynamic analysis, a static analysis of the specimen is performed to obtain the critical load-point deflection which produces the initiation stress intensity factor $K_{IQ} = 224$ MNm$^{-1.5}$ at the crack tip. Then the crack starts propagating dynamically from this initial static state of the specimen. The static stress intensity factor as well as dynamic stress intensity factors during the crack propagation are obtained

directly by the present singularity element procedure as described earlier.

In the experiment [4], the specimen was loading in a testing machine by forcing a 20-degree wedge between the pins as shown in Fig. 3a. After crack initiation the wedge was fixed at the same position. Obviously the wedge can "push" the pins attached to the specimen but not "pull" them. Thus there is the possibility of a lack of contact of the specimen (pins) with the wedge (see Fig. 3b). In one case, the wedge loading condition taking account of the above effect of no-contact is considered, while, in other cases, the fixed loading condition, i.e., one in which the wedge is always in contact with the pins, is used.

Using the standard notation, the reaction forces at the points where displacements are prescribed are calculated by:

$$\underset{\sim}{P} = \underset{\sim}{K}\underset{\sim}{q} + \underset{\sim}{m}\ddot{\underset{\sim}{q}}$$

The displacement u and reaction force P in the time step (n+1) are predicted by:

$$u_{n+1} = u_n + \Delta t_{n+1}\dot{u}_n \tag{6}$$

$$P_{n+1} = P_n + \frac{(P_n - P_{n-1})}{\Delta t_n} \Delta t_{n+1} \tag{7}$$

It is noted that we may use $\Delta t_{n+1} = \Delta t_n = \Delta t$.

We designate the reaction forces with which the wedge pushes the pins as being positive. Thus in Fig. 3a, both the reaction forces acting on the upper and lower pins are positive. The no-contact condition during the time increment (n) to (n+1) is predicted to occur after the sub-increment of time:

$$\Delta t_c = \frac{P_n}{(P_{n-1} - P_n)} \Delta t \tag{8}$$

If $0 \leq \Delta t_c \leq \Delta t$, during the (n+1) step we change Δt to Δt_c and perform the analysis

- 6 -

with the condition of contact, and during (n+2) step, we change Δt to Δt_F ($=\Delta t-\Delta t_c$) and perform the analysis with the condition of no-contact (free).

An analogous scheme is used to predict the transition form no-contact to contact conditions. By monitoring the displacement, the sub-increment of time to reestablish contact is predicted by:

$$\Delta t_F = \frac{-\delta_L}{\dot{\delta}_L} \qquad (9)$$

where $\delta_L = u_L - \bar{u}_L$. If $0 \leq \Delta t \leq \Delta t_F$, during the (n+1) step we change Δt to Δt_F and perform the analysis with the no-contact condition, and during the (n+2) step we change Δt to Δt_c ($=\Delta t-\Delta t_F$) and perform the analysis with the contact condition. These schemes are repeated for the entire computation.

The high strength maraging steel HFX760 was chosen in the experiment [4]. Reference [4] has indicated that the steel has a yield strength of σ_{ys}=2.1 GN/m^2, a crack initiation toughness K_{IC} in the range of 70 to 100 MNm$^{-1.5}$, and a bar wave speed of C_o=5190 m/sec. However reference [4] has not indicated any other material properties such as Young's modulus E, Poisson's ratio ν and the mass density ρ which are required in an elastodynamic analysis. To investigate the effect of material properties on crack propagation and arrest in the DCB specimen, four different hypothesized material-properties, as listed in Table 1, are used in the present analysis.

Results and Discussions

(i) Fixed Loading (Prescribed Displacement; wedge always in contact with specimen)

First we consider the Material I case. The variation of dynamic stress intensity factor computed in the present generation phase simulation is shown in Fig. 4. The time increment Δt used in the present analysis is 1.5 μsec. After 183 μsec. the simulation was continued with three different crack extension histories, i.e., Data 1, Data 2, and Data 3. As seen from the figure, in the

Data 1 case, the dynamic stress intensity factors continuously decrease before the crack arrest. On the other hand in the Data 2, and Data 3 cases, the stress intensity factors increase just before the crack arrest. Obviously, the Data 1 case is the most realistic. The crack arrest toughness K_{Ia} in this case for Material I is obtained as 55.3 $MNm^{-1.5}$. The range for the crack initiation toughness K_{Ic} is also shown in Fig. 4. K_{Ia} value appears to be lower than the crack initiation toughness K_{Ic}. Notations D_A, S_C, D_B and R_A will be explained later.

The presently obtained K-values for Material I are shown in Fig. 5 along with those measured in the experiment [4]. The experimental results show large oscillations for the period of the crack length of 100 mm to 190 mm. After this period the experimental results become smoother. The present result is very close to the experimental results during the period of $\Sigma \geq 190$ mm, and close to the lower bound of the experimental oscillations during 100 mm $\leq \Sigma \leq 190$ mm.

As mentioned earlier, in the authors' opinion, these oscillations in the experiment may be due to the high frequency vibration of the surface of the steel specimen. Although a three-dimensional analysis is required to investigate the effects of the surface vibrations, inside the thickness of this thin specimen, a "generalized plane stress" two-dimensional analysis may be seen to be valid. In comparing both the results it seems plausible that this vibration occurs only on the surface of the specimen.

The computed variations of input energy W, strain energy U, kinetic energy T, and fracture energy F are shown in Fig. 6. It is noted that in the present procedure the dynamic K_I-value is calculated directly as a variable in the finite element equations [5,6]. The fracture energy is thus calculated directly by integrating the energy release rate based on the present K_I-value. Alternatively,

fracture energy is also calculated directly from a crack-tip integral of work done in separation of crack-faces. These two procedures gave almost identical results in the present analyses.

Since the input energy to the specimen W is a constant in the present case, the above computed F, U, and T should add up to a constant. It is seen that the error in (F+U+T) as compared to W increases almost linearly from 0.0% to 3.3% towards the end of crack propagation. Since this analysis was carried out in 140 time steps, it is reasonable to presume that the error in each time step is thus roughly 0.02%. This appears to give enough credence to the presently computed stress intensity factors for this type of specimen. In other types of specimen such as dynamic tear test specimen [9], however, it was found that the total output energy (F+U+T) is almost identical to the input energy W during the analysis carried out in 360 time steps. It is seen from Fig. 6 that about 88% of input energy is consumed as fracture energy in the present steel DCB specimen. The strain energy U continuously decreases up to the time of crack arrest. Contrary to this, the kinetic energy T, takes its maximum value as 28.9% of the total input energy at the earlier stage of the crack propagation, and becomes negligible at crack arrest.

Next we consider the Material II case. Fig. 7 shows the variation of dynamic stress intensity factors. In the Data 1 and Data 2 cases the stress intensity factors take the minimum values before crack arrest. The minimum K_I-value in the Data 1 case is 40.5 $Mnm^{-1.5}$ which is considerably lower than K_{Ia} in the Material I case. Fig. 8 shows the K_I-value as a function of crack length. For the crack length values of 100 to 190 mm, the present results agree well with the lower bound of the experimental data. The variations of the total work, strain energy, kinetic energy, and fracture energy are shown in Fig. 9. The maximum kinetic energy in this case is 25.6% of the total input energy, which

is lower than that in the Material I case.

Now we consider the Material III case. In this case, only Poisson's ratio is different from that in the Material I case. The variation of dynamic stress intensity factors is shown in Fig. 10. The results are very close to those in the Material I case. The K_I-value as a function of crack length and the energy variation in this specimen are respectively shown in Figs. 11 and 12. Again the results are very close to those in the Material I case.

Finally, we consider the Material IV case. In this case only the mass density is different and 14% higher than that in the Material II. The variation of dynamic stress intensity factors is shown in Fig. 13. The crack arrest toughness K_{Ia} obtained for this specimen using Data 1 is 51.0 MNm$^{-1.5}$, which is about 8% lower than that in the Material I case. Fig. 14 shows dynamic K_I-value as a function of crack length. For the crack length of 100 to 190 mm, the present K_I-value variation is lower than the lower bound of oscillation of the experimental data, while for $\Sigma \geq 190$ mm the present results agree excellently with the experimental results. Fig. 15 shows the energy variations. The maximum kinetic energy obtained in this specimen is 28.1% of the total input energy.

The maximum kinetic energies and the crack arrest toughness obtained for the four cases are summarized in Table 2. A good correlation between the inertia effect (the ratio of the maximum kinetic energy to input energy) and crack arrest toughness, i.e., the increasing K_{Ia} with the increasing ratio of the maximum kinetic energy to input energy [(max T)/W] can be observed in Table 2.

The influence of Poisson's ratio on dynamic stress intensity factors is shown in Fig. 16, comparing directly the Material I and II cases. Almost identical variations of stress intensity factor can be seen in Fig. 16 for the two cases of ν. On the contrary, a large effect of Poisson's ratio on crack propagation

and arrest in DCB specimen has been reported in Ref. [12]. The author of Ref.
[12] has claimed that for any given geometry, different materials are distinguished
in the finite difference scheme by their correspondingly different Poisson's
ratio only. This is quite different from the situation in any other numerical
schemes such as the finite element method and so on. This is also different
from the situation in elastostatic analysis. To expain the claim, the author
in Ref. [12] described that all physical quantities in the problem were given
relative to the specimen height H, the dilatational wave velocity C_1, and the
material density ρ. The distortional wave velocity C_2 was defined in terms
of C_1 according to the relation $C_2 = C_1 \sqrt{(1-2\nu)/(2-2\nu)}$. From this, the claims
mentioned above was derived. However this explanation does not appear correct,
since the dilatational wave velocity C_1 cannot be a basic unit. The velocity
C_1 depends not only on the Poisson's ratio and mass density but also on the
Young's modulus, since C_1 is expressed as

$$C_1 = \sqrt{\frac{E(1-\nu)}{\rho(1+\nu)(1-2\nu)}}$$

under the plane strain condition assumed in Ref. [12]. If Poisson's ratio is
changed with keeping $C_1 = 1$ and $\rho = 1$, Young's modulus is also changed according
as:

$$E = \frac{(1+\nu)(1-2\nu)}{(1-\nu)}$$

Therefore the dynamic effect shown in Ref. [12] includes the effects of Young's
modulus as well as Poisson's ratio.

The influence of the Young's modulus on dynamic stress intensity factors
is shown in Fig. 17. The result shown by the solid line for $\nu = 0.3$ was obtained
by taking the average of K_I-values for $\nu = 0.318$ (Material I) and $\nu = 0.280$ (Material
II). The figure indicates that the dynamic effect in the specimen of E=183 GPa
(Material I) is larger than that in the case of E=190 GPa (Material IV). This

- 11 -

means that the dynamic effect increases with the decreasing Young's modulus. This tendency can also be found in Table 2, i.e., the ratio of maximum kinetic energy to input energy in Material I (E=183 GPa) is larger than that in Material IV (E=190 GPa).

The influence of mass density on the dynamic stress intensity factors is shown in Fig. 18. The figure indicates that the dynamic effect increases with the increasing mass density. Again this tendency can be observed on Table i.e., the ratio of maximum kinetic energy to input energy in Material IV (ρ= 8042 kg/m^3) is larger than that in Material II (ρ=7053 kg/m^3).

For all cases considered here, at the beginning of the crack propagation, the dynamic stress intensity factors decrease drastically, and then become constant for a while. At about a half of the crack propagation histories, the present stress intensity factor variations exhibit their peaks. To investigate these phenomena, the times for various waves, generated from the fast crack initiation and reflected from boundaries, to interact with the propagating crack-tip are computed and shown in Figs. 4, 7, 10, and 13. With A, B, and C denoting the three boundaries as marked in Fig. 1, D_B and D_C are the times when the dilatational waves reflected from the boundaries B and C, respectively, interact with the propagating crack-tip. Similar notations are used for R_A and S_C denoting respectively the Rayleigh wave reflected from the boundary A and the shear wave reflected from the boundary C. It is interesting to note that the K_I-value begins to be constant at the time D_C, and begins to peak at the time D_B. It is also seen that the peak in the variation of K_I-value occurs shortly after the time R_A. Effects of Rayleigh waves in dynamic crack propagation have also been studied in Ref. [7,13,14].

Furthermore, to investigate the effect of Rayleigh wave on dynamic fracture, the Rayleigh wave velocities C_R are also listed in Table 2. It is seen that the Rayleigh wave velocity has good correlations with both the ratio of maximum

- 12 -

kinetic energy to input energy, and the crack arrest toughness.

(ii) <u>Wedge Loading (Contact/No-contact)</u>

For the Material I, the variation of reaction force at the loading point
where the displacement is prescribed during the crack propagation is shown in
Fig. 19. The reaction force becomes zero at t=60 μsec, and then oscillates
with decreasing amplitude. A negative reaction force is observed during time
periods 60 μsec to 100.5 μsec, 129 μsec to 171 μsec, 187.5 μsec to 202.5 μsec,
and so on. This phenomenon can also be observed in the reaction force variation
in t$^+$ dynamic tear test specimen [9]. During the periods of negative reaction
force, the wedge is not pushing but pulling the specimen (pins). This situation
is not realistic in the mechanism of the wedge loading.

The variation of crack opening displacements during the crack propagation
is shown in Fig. 20. Since the displacement at the loading point of x=16 mm
and y=20 mm is always fixed, the beam parts of the specimen rotate around this
point due to the crack extension. The variation of crack-face profiles indicates
this rotation.

To simulate a more realistic mechanism of the wedge loading, the conditions
of contact/no-contact are invoked in the present analysis. The variations of
reaction force, and the distance between the wedge and the point L are shown in
Fig. 21. L_1 as shown in Fig. 21 is the time when the reaction force becomes
zero. As seen from the figure, the specimen is not in contact with the wedge
after L_1 (=60 μsec). The distance between the wedge and the point L, $u_L - \bar{u}_L$,
becomes larger and larger with time.

The variation of crack opening displacements with the condition of contact/
no-contact is shown in Fig. 22. In contrast to the crack-face profiles for
the fixed loading case as shown in Fig. 20, it can be seen from Fig. 22 that
the variation of the crack-face profiles shows the parallel movement of the
beam parts of the specimen after the no-contact condition occurs at t=60 μsec.

- 13 -

Fig. 23 shows the comparison of the dynamic stress intensity factors obtained with the different loading conditions. In comparing the both results, it is seen that the K_I-values calculated with the wedge (contact/no-contact) loading, are exactly same before 60 μsec, almost identical during the time of 60 μsec to about 120 μsec, and lower during the time of 120 μsec to 210 μsec. The effect of the no-contact condition on dynamic stress intensity factor starts manifesting roughly 60 μsecs after the condition of no-contact occurs. This is due to the time-lag in which the "no-contact" effect propagates from the point L to the running crack-tip. To further investigate the propagation speed of this effect, the arrival times of the elastic waves emanating from the loading point are examined. D_L and S_L as shown in Fig. 23 are, respectively, the arrival times of the dilatational and shear waves, emanated from point L, at the crack-tip. It is seen that the no-contact effect at the crack-tip begins to manifest itself at the instant S_L while no effect can be seen at the time D_L. In the wedge loading (contact/no-contact) case, a slightly lower crack arrest toughness was obtained as 54.2 Mnm$^{-1.5}$.

Fig. 24 shows the variation of the energies obtained from the present analysis with the condition of contact/no-contact. The kinetic energy variation after 120 μsec appears to be higher than that in the fixed loading case as shown in Fig. 6. This higher kinetic energy is due to the movement of the beam parts of the specimen away from the wedge.

Summary and Conclusion:

Utilizing the moving-singularity element procedure, finite element simulations of fast fracture in high strength steel DCB specimen have been performed for different material properties, different crack propagation histories, and different loading conditions.

The major conclusions and observations obtained from this study are summarized below:

(1) The dynamic crack propagation and arrest are influenced, largely by the
mass density, moderately by the Young's modulus, and almost negligibly by
the Poisson's ratio.

(2) The variation of dynamic stress intensity factors is influenced by the
various waves originally generated from the fast crack initiations and
then reflected from the boundary of the specimen.

(3) The ratio of the maximum kinetic energy to the input energy increases with
the decreasing Rayleigh wave velocity.

(4) The crack arrest toughness, for a given crack propagation history, increases
with the increasing ratio of the maximum kinetic energy to the input
energy, or with the decreasing Rayleigh wave velocity.

(5) Analysis with a realistic wedge loading condition (contact/no-contact) gives
a slightly lower variation of stress intensity factors than that with the
fixed loading condition (speciment always in contact with the wedge). Ef-
fects of the different loading conditions depend on the initial crack length
and crack velocity. This contact/no-contact effect propagates with a speed
of the order of shear wave velocity. Thus, if a larger initial crack length
is used, this effect appears at the crack-tip much later.

Acknowledgements:

Reference:

(1) Kalthoff, J.F., Beinert, J., and Winkler, S., "Measurements of Dynamic
Stress Intensity Factors for Fast Running and Arresting Cracks in Double-
Cantilever-Beam Specimens", Fast Fracture and Crack Arrest, ASTM STP 627
(G.T. Hahn and M.F. Kanninen, Eds.), American Society for Testing and
Materials, 1977, pp. 161-176.
(2) Klathoff, J.F., Winkler, S., and Beinert, J., "The Influence of Dynamic

Effects in Impact Testing", _International Journal of Fracture_, Vol. 13,
1977, pp. 528-531.

(3) Kalthoff, J.F., Beinert, J., Winkler, S., and Blauel, J.G., "On the
Determination of the Crack Arrest-Toughness", _Fracture_, (D.M.K. Taplin,
Ed.), University of Waterloo Press, 1977, Vol. 3, pp. 751-756.

(4) Kalthoff, J.F., Beinert, J., Winkler, S., and Klemm, W., "Experimental
Analysis of Dynamic Effects in Different Crack Arrest Test Specimens", a
paper presented at the ASTM E-24 Symposium on Crack Arrest Methodology and
Applications, Philadelphia, Nov. 6-7, 1978.

(5) Atluri, S.N., Nishioka, T., and Nakagaki, M., "Numerical Modeing of Dynamic
and Nonlinear Crack Propagation in Finite Bodies by Moving Singular-Elements",
Nonlinear and Dynamic Fracture Mechanics, ASME AMD, Vol. 35, (N. Perrone
and S.N. Atluri, Eds.), New York, 1979, pp. 37-67.

(6) Nishioka, T., and Atluri, S.N., "Numerical Modeling of Dynamic Crack
Propagation in Finite Bodies, by Moving Singular Elements, Part I:
Formulation", _Journal of Applied Mechanics_, Vol. 47, No. 3, 1980, pp.
570-576.

(7) Nishioka, T., and Atluri, S.N., "Numerical Modeling of Dynamic Crack
Propagation in Finite Bodies, by Moving Singular Elements, Part II:
Results", _Journal of Applied Mechanics_, Vol. 47, No. 3, 1980, pp. 577-583.

(8) Nishioka, T., and Atluri, S.N., "Numerical Analysis of Dynamic Crack
Propagation: Generation and Prediction Studies", to be published in
Engineering Fracture Mechanics.

(9) Nishioka, T., Perl, M., and Atluri, S.N., "An Analysis of, and Some Obser-
vation on, Dynamic Fracture in an Impact Test Specimen", ASME paper 81-PVP-
18, presented in ASME Pressure Vessels and Piping Conference, Denver, CO,
June 21-25, 1981.

(10) Voss, B., and Blauel, J.G., "Zur Korrelation der Bruchzähigkeit mit
Kennwerten aus Zug-, Kerbzug- und Biegeversuch", Deutscher Bergand fur
Materialprüfung e.V., 9. Sitzung des Arbeitskreises Bruchvorgange, 12.10.
1977, Berlin, pp. 107-122.

(11) Kalthoff, J.F., Private Communication to M. Perl, Institut fur Frestkörpermechanik
der Fraunhofer-Gesellschaft, Freiburg, Germany.

(12) Shmuely, M., "Effect of Poisson's Ratio on Crack Propagation and Arrest
in the Double-Cantilever-Beam Specimen", _Fast Fracture and Crack Arrest_,
ASTM STP 627, (G.T. Hahn and M.F. Kanninen, Eds.), American Society for
Testing and Materials, 1977, pp. 135-141.

(13) Nishioka, T., and Atluri, S.N., "Efficient Computational Techniques for the
Analysis of Some Problems of Fracture in Pressure Vessels and Piping", ASME
Paper 80-C2/PVP-110, presented in the Century 2 Pressure Vessels and Piping
Conference, San Fransisco, CA, August 12-15, 1980.

(14) Shmuely, M., Peretz, D., and Perl, M., "Effect of Rayleigh Waves in Dynamic
Fracture Mechanics", _International Journal of Fracture_, Vol. 14, 1978, technical
notes, R69-R72.

Captions for Figures and Tables:

Table 1: Material Property Data for Different Cases

Table 2: Dynamic Effects on crack arrest toughness

Fig. 1: Finite element model for a double-cantilever-beam specimen.

Fig. 2: Crack propagation history and crack velocity history as input data to generation phase fracture simulation.

Fig. 3: Contact/no-contact conditions between wedge and pins.

Fig. 4: Variation of dynamic stress intensity factors (Material I).

Fig. 5: Dynamic stress intensity factors versus crack length (Material I).

Fig. 6: Energy variations (Material I).

Fig. 7: Variation of dynamic stress intensity factors (Material II).

Fig. 8: Dynamic stress intensity factors versus crack length (Material II).

Fig. 9: Energy variations (Material II).

Fig. 10: Variation of dynamic stress intensity factors (Material III).

Fig. 11: Dynamic stress intensity factors versus crack length (Material III).

Fig. 12: Energy variations (Material III).

Fig. 13: Variation of dynamic stress intensity factors (Material IV).

Fig. 14: Dynamic stress intensity factors versus crack length (Material IV).

Fig. 15: Energy variations (Material IV).

Fig. 16: Influence of Poisson's ratio on dynamic crack propagation and arrest.

Fig. 17: Influence of Young's modulus on dynamic crack propagation and arrest.

Fig. 18: Influence of mass density on dynamic crack propagation and arrest.

Fig. 19: Variation of reaction force between wedge and pins during the crack propagation (fixed loading condition).

Fig. 20: Variation of crack-face profiles (fixed loading condition).

Fig. 21: Variations of reaction force and distance between wedge and pin L (wedge loading condition: contact/no-contact).

Fig. 22: Variation of crack-face profiles (wedge loading condition).

Fig. 23: Influence of the loading conditions on dynamic crack propagation and arrest.

Fig. 24: Energy variations with the wedge loading condition.

Table 1

(Data 1)

Material Number	Young's Modulus $E[GN/M^2]$	Poisson's Ratio ν	Mass Density $\rho[kg/m^3]$	Bar Wave Speed $\sqrt{E/\rho}$ [m/sec]
I	183[a]	0.318[a]	8042[a]	4770
II	190[b]	0.3[c]	7053[d]	5190
III	183	0.280	8042	4770
IV	190	0.3	8042	4860

(a) Obtained from J.F. Kalthoff [11].

(b) Taken from Ref. [10].

(c) Assumed.

(d) Calculated by $\rho = E/C_o^2$; $C_o = 5190$ m/sec.

Table 2

Material Number	Maximum Kinetic Energy/Input Energy (Max.T)W [%]	Crack Arrest Toughness* K_{Ia} [MNm$^{-1.5}$]	Rayleigh Wave Velocity C_R [m/sec]
I	28.9	55.3	2730
II	25.6	45.7 (40.5)**	2980
III	28.8	54.8	2750
IV	28.1	51.0	2790

*   Obtained for Data 1 case.

**   Minimum K-value in this case.

LENGTH W = 321 mm
HEIGHT H = 127 mm
THICKNESS B = 9 mm

INITIAL
CRACK
LENGTH $\Sigma_0 =$ 67.8 mm
l = 16 mm
h = 20 mm

Fig. 1

Fig. 2

CONTACT (if $P_L > 0$)

(a)

NO-CONTACT (if $u_L > \bar{u}_L$)

(b)

Fig. 3

HIGH STRENGTH STEEL
HFX 760
$K_{1Q} = 224$ MNm$^{-1.5}$

Generation Phase
Plane Stress
Material 1

• Present K_I - Value

—o— Input Data
$(\Sigma = \Sigma(t) ; \upsilon = \upsilon(t))$

Fig. 4

HFX · 760
MATERIAL I
DATA I

— PRESENT

⊙ EXPERIMENT (Kalthoff et al)
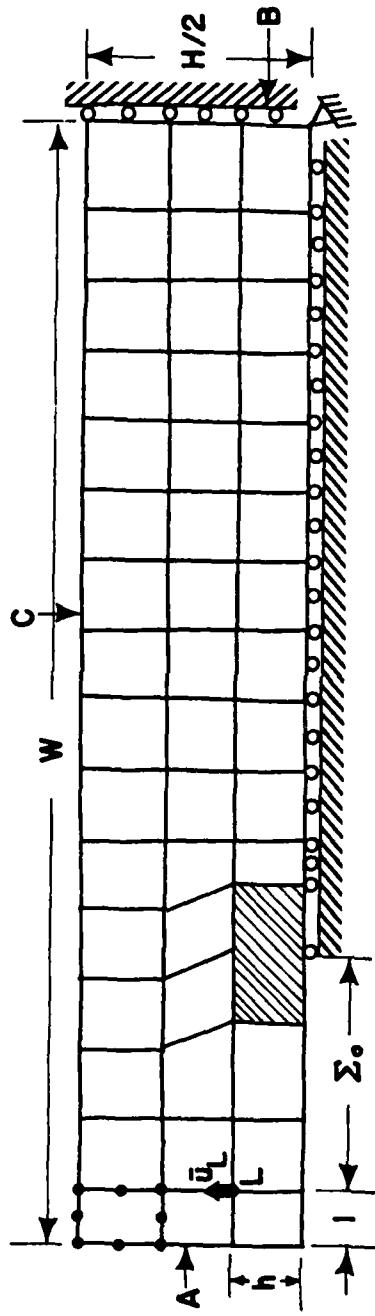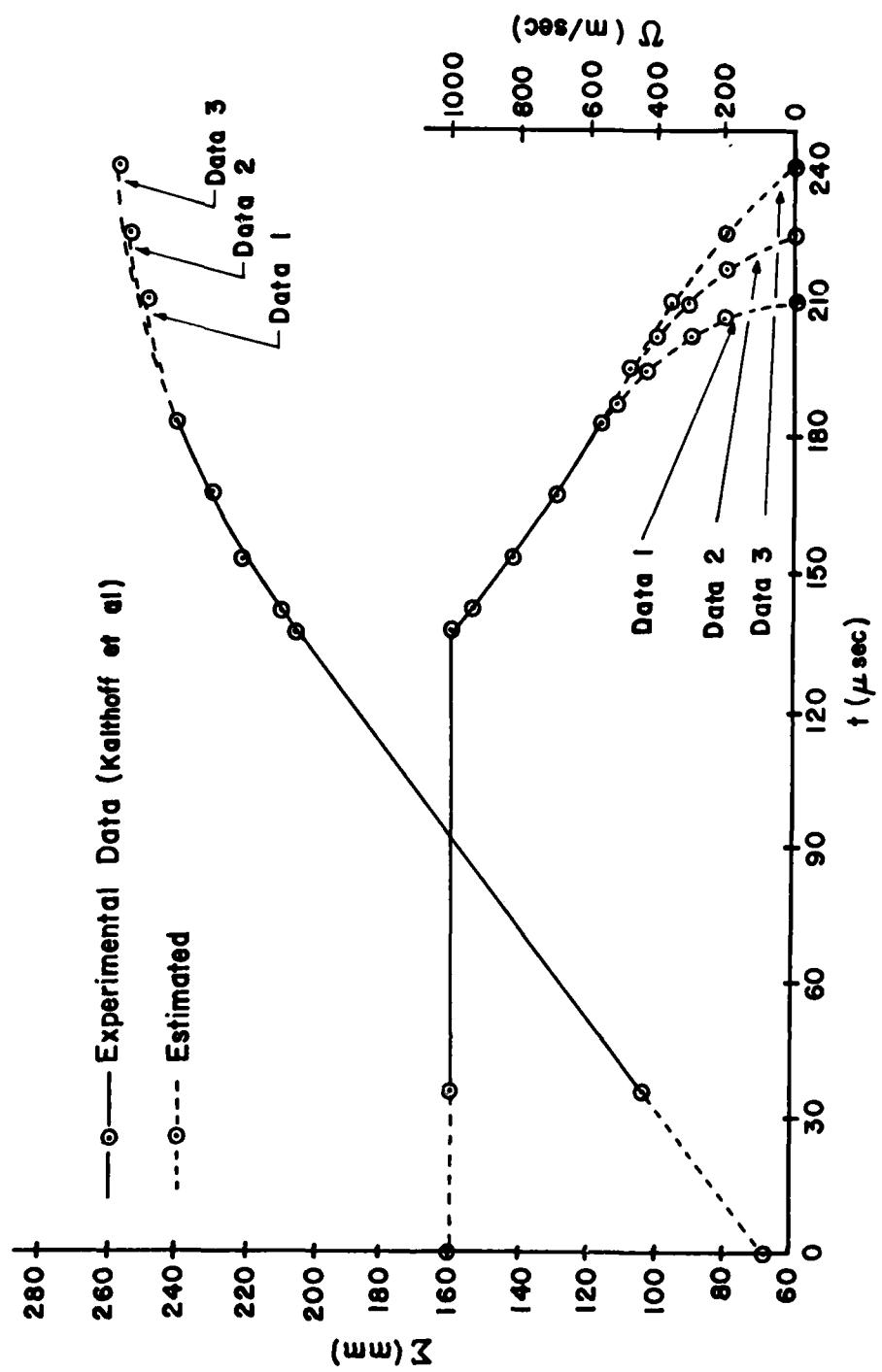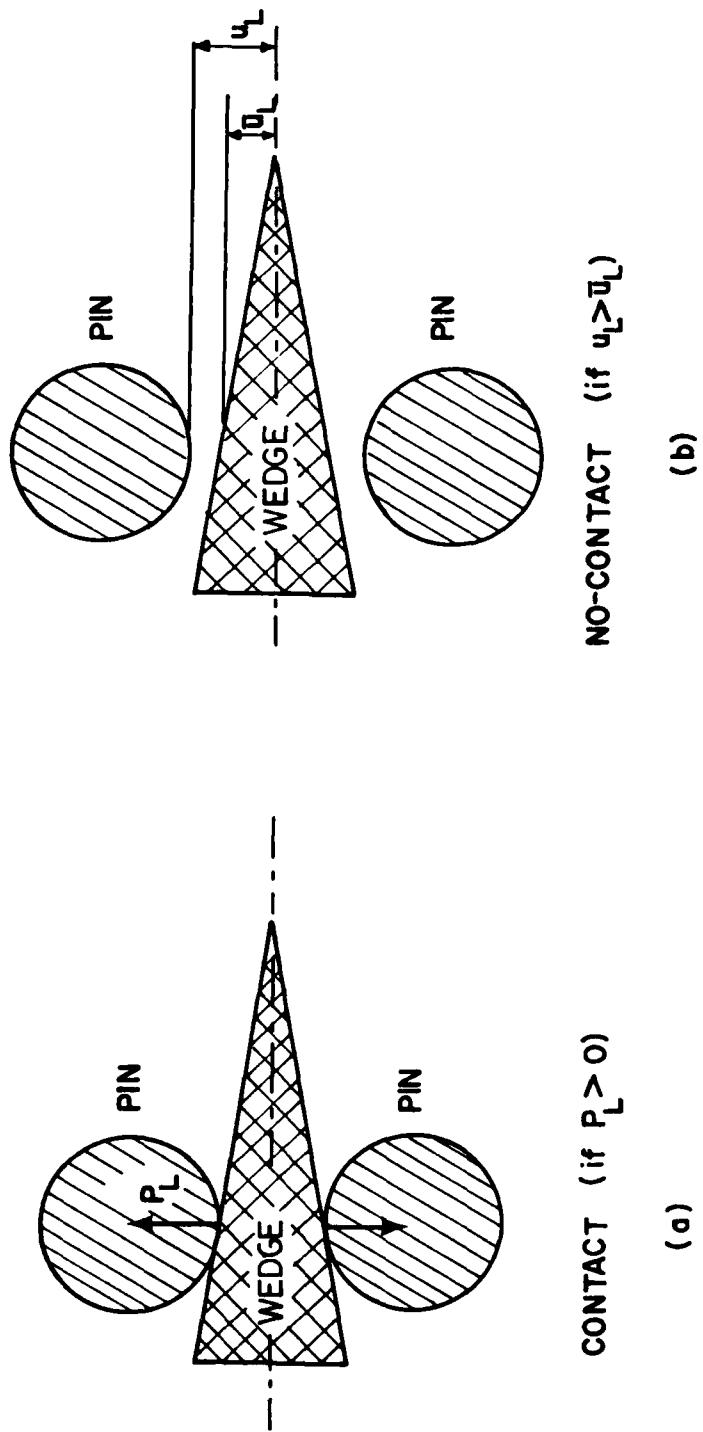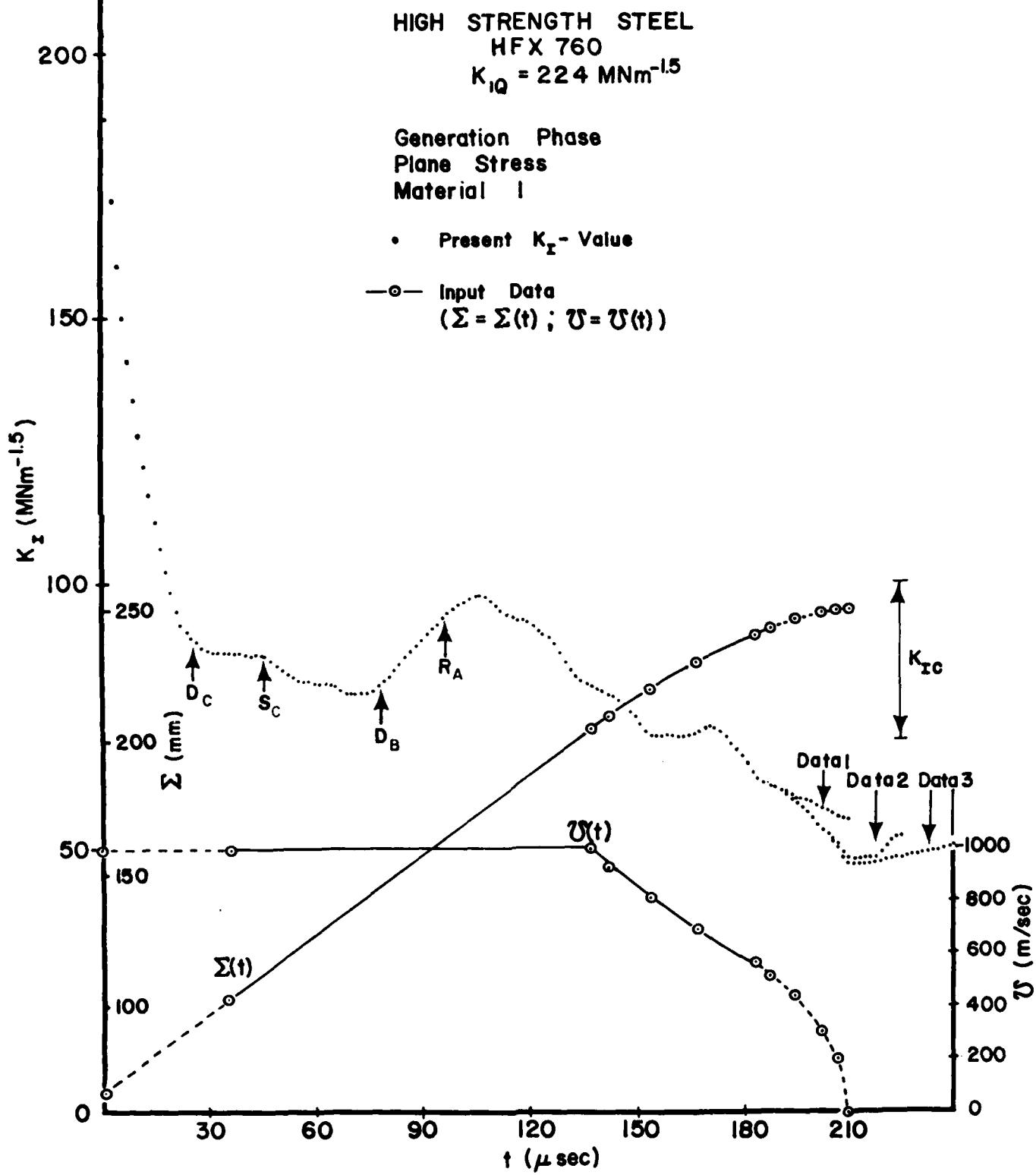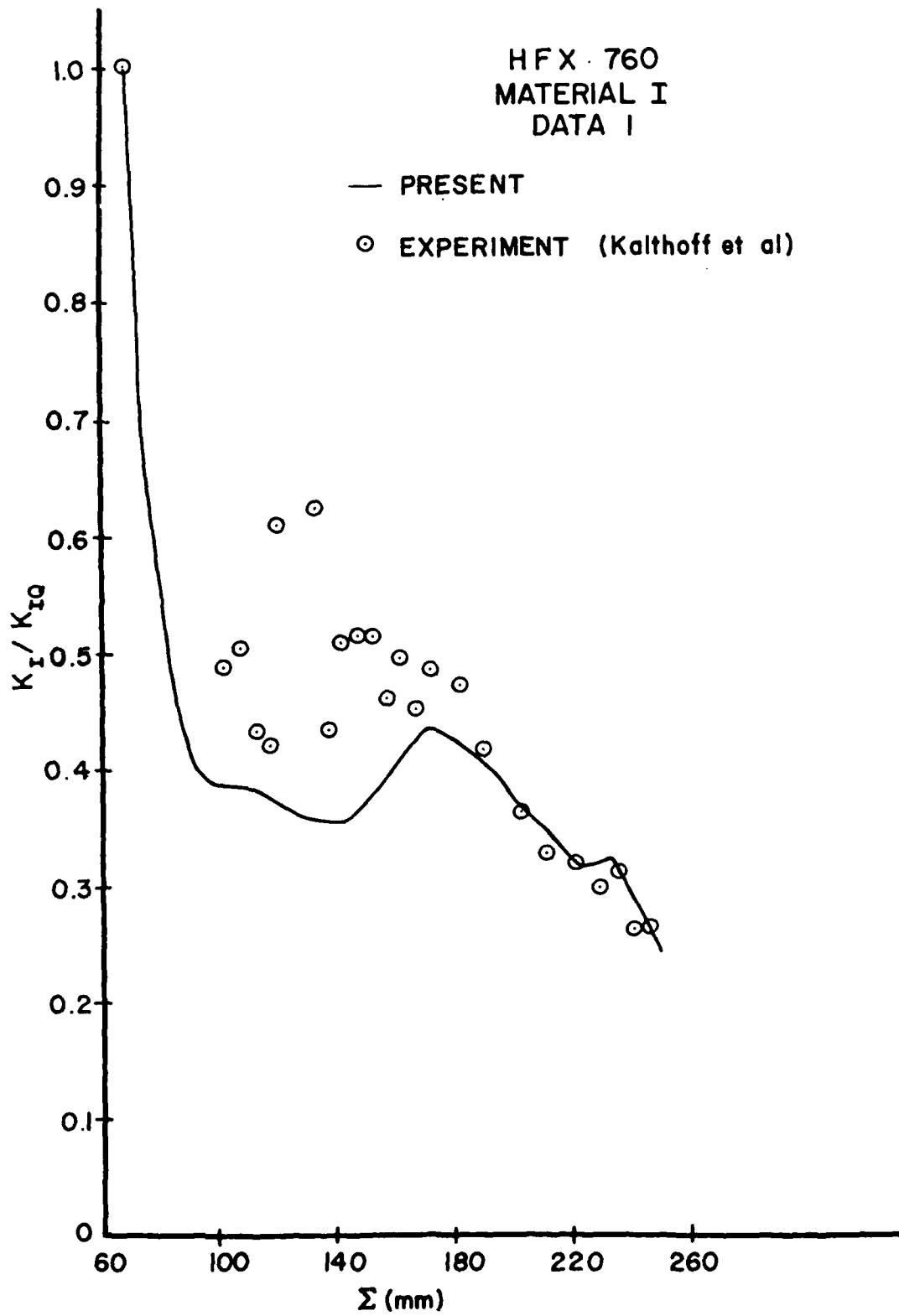
Fig. 5

HFX 760
MATERIAL I , DATA I

Fig.6

Fig. 7

HFX 760
MATERIAL II
DATA I

—— PRESENT

⊙ EXPERIMENT (Kalthoff et al)

K_I / K_{Ia}

Σ (mm)
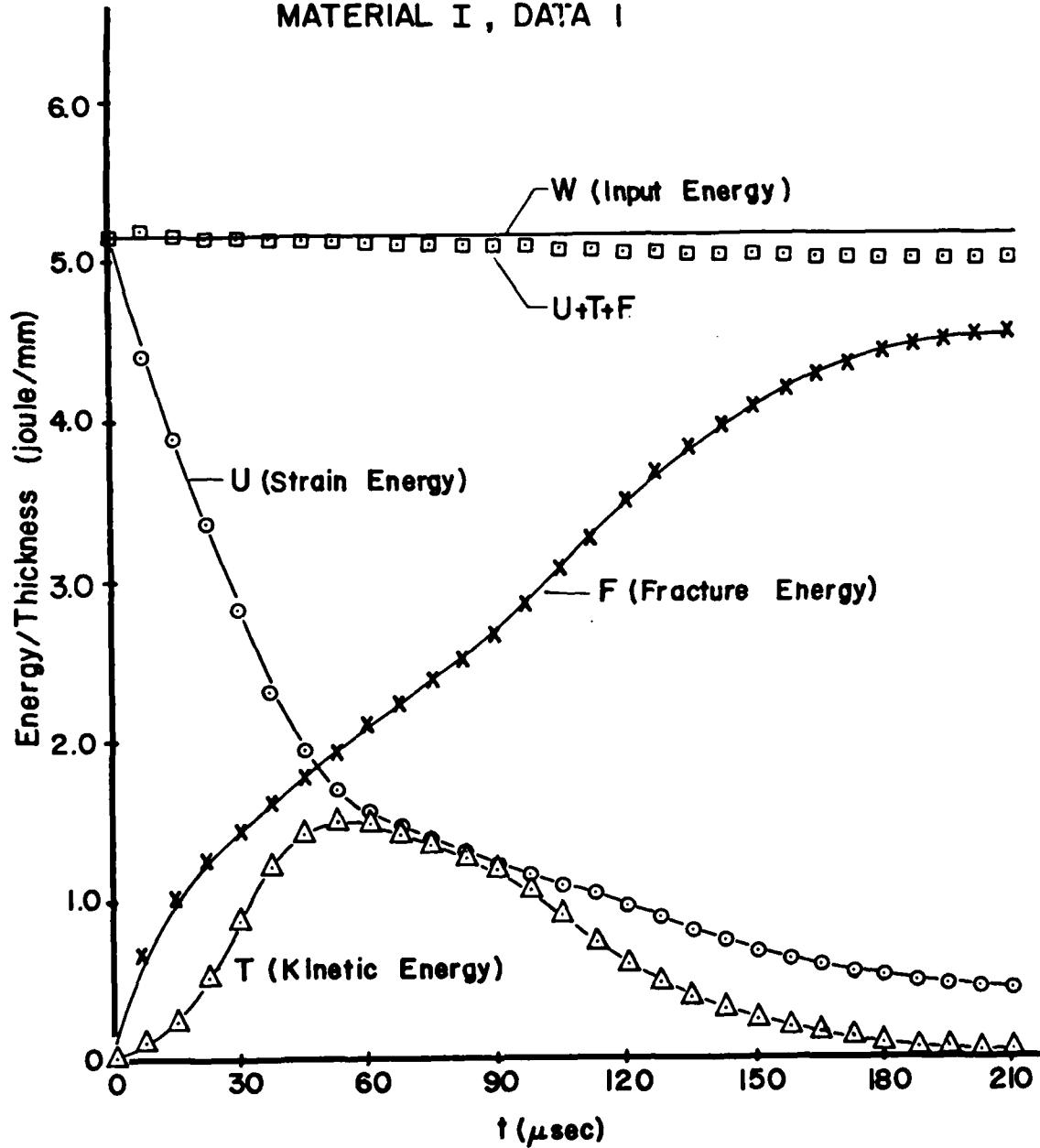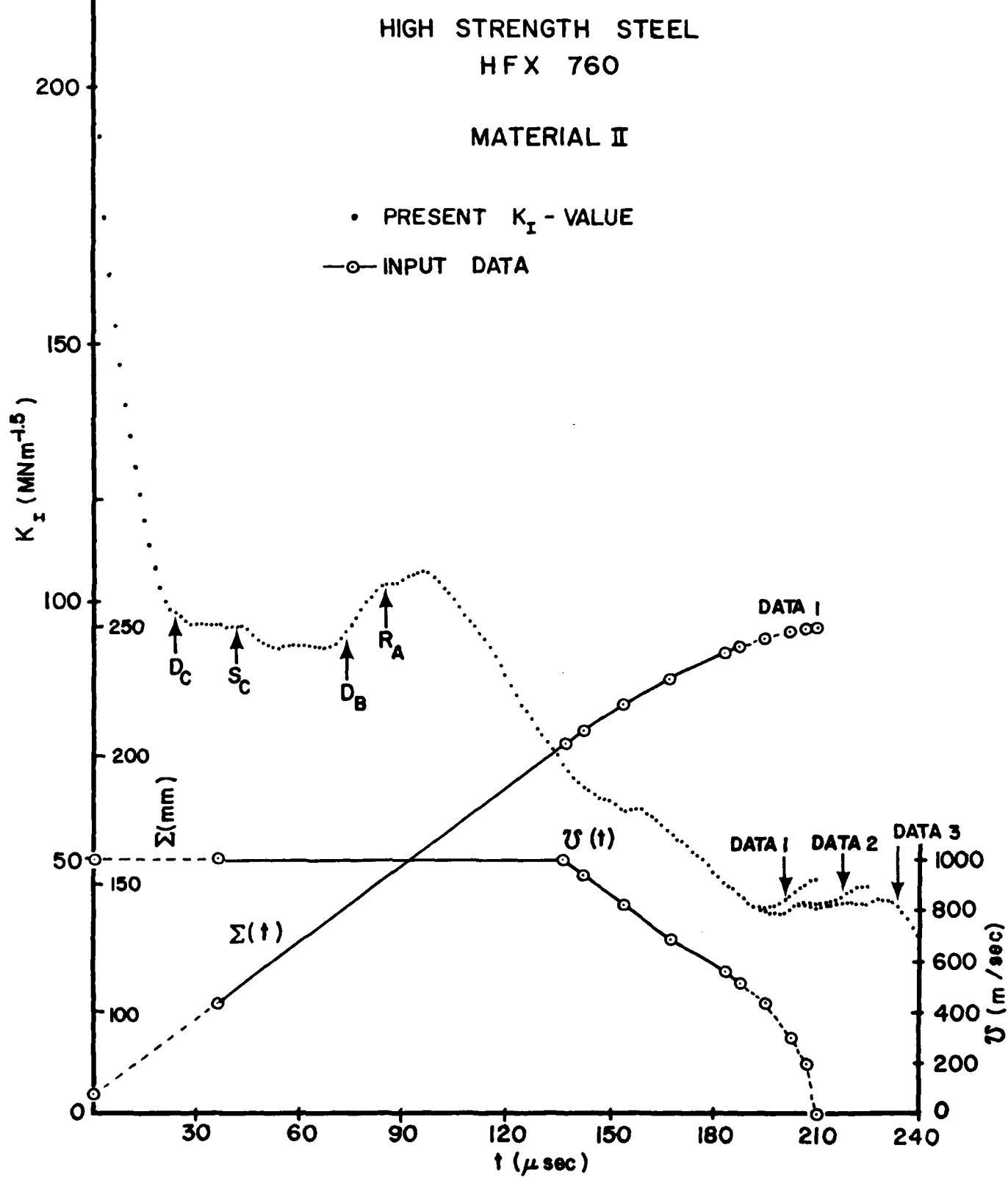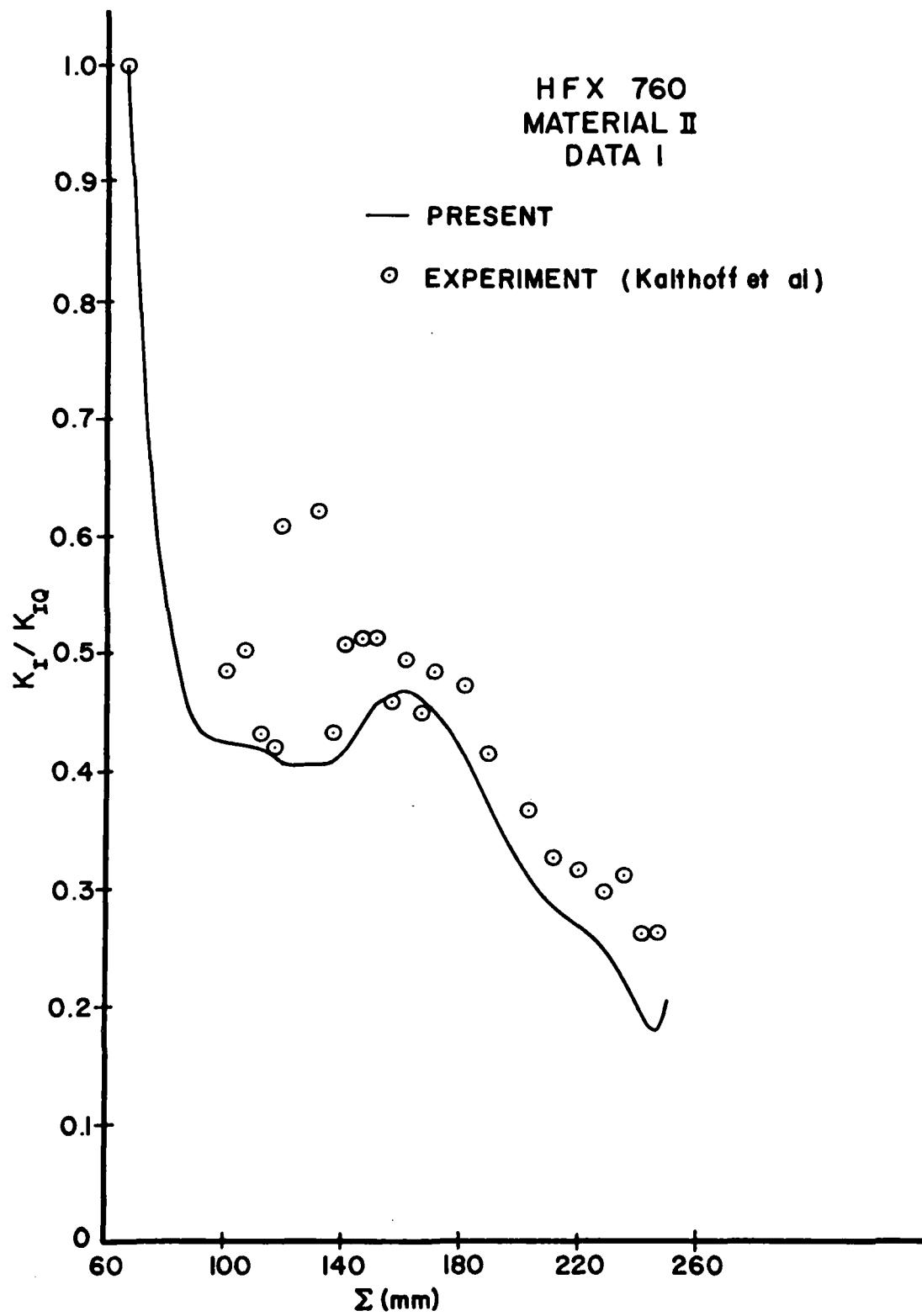
Fig. 8

HFX 760
MATERIAL II, DATA

Fig. 9

Fig. 10

HFX 760
MATERIAL III
DATA I

—— PRESENT

⊙ EXPERIMENT (Kalthoff et al)
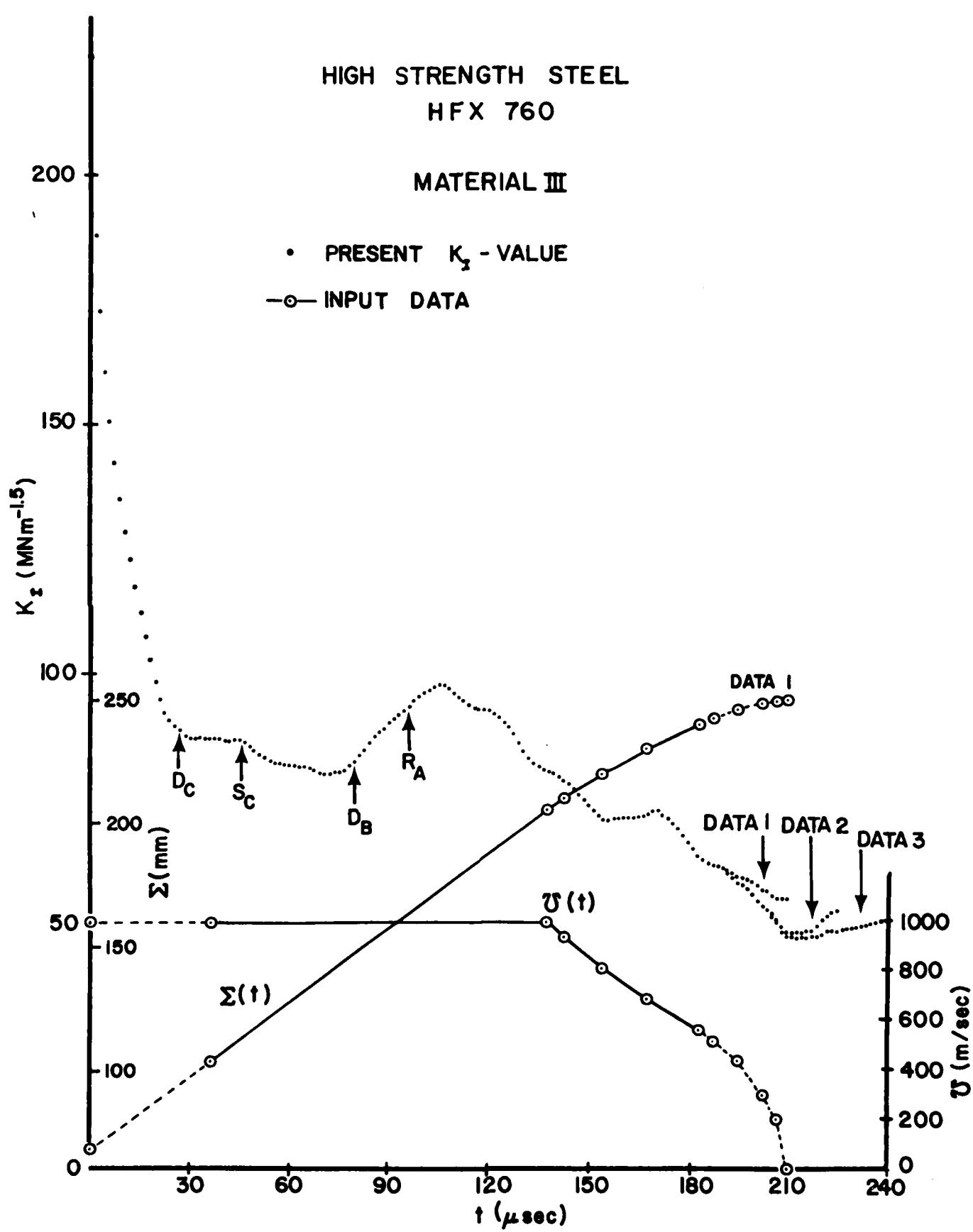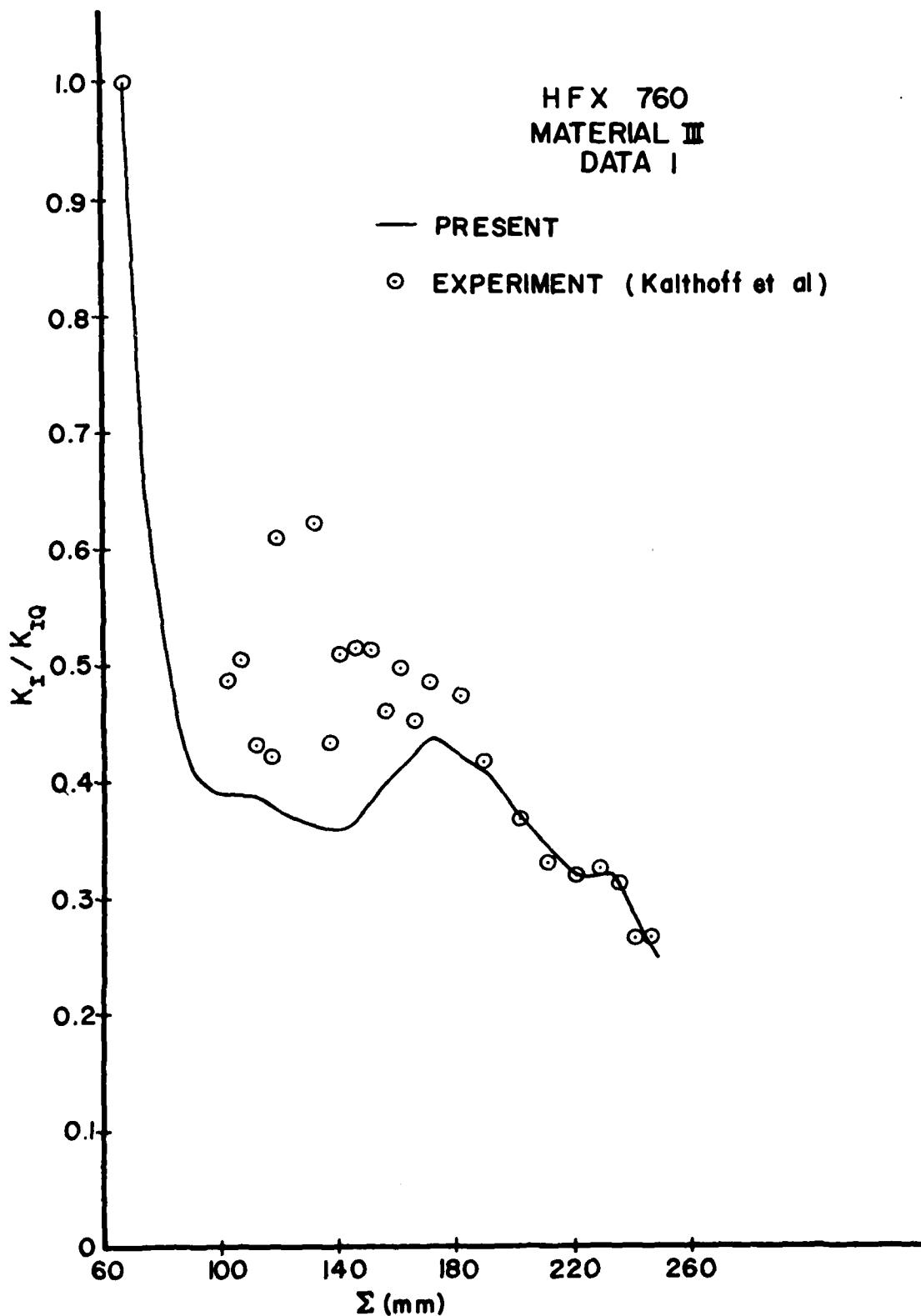
Fig. 11

HFX 760
MATERIAL Ⅲ, DATA I
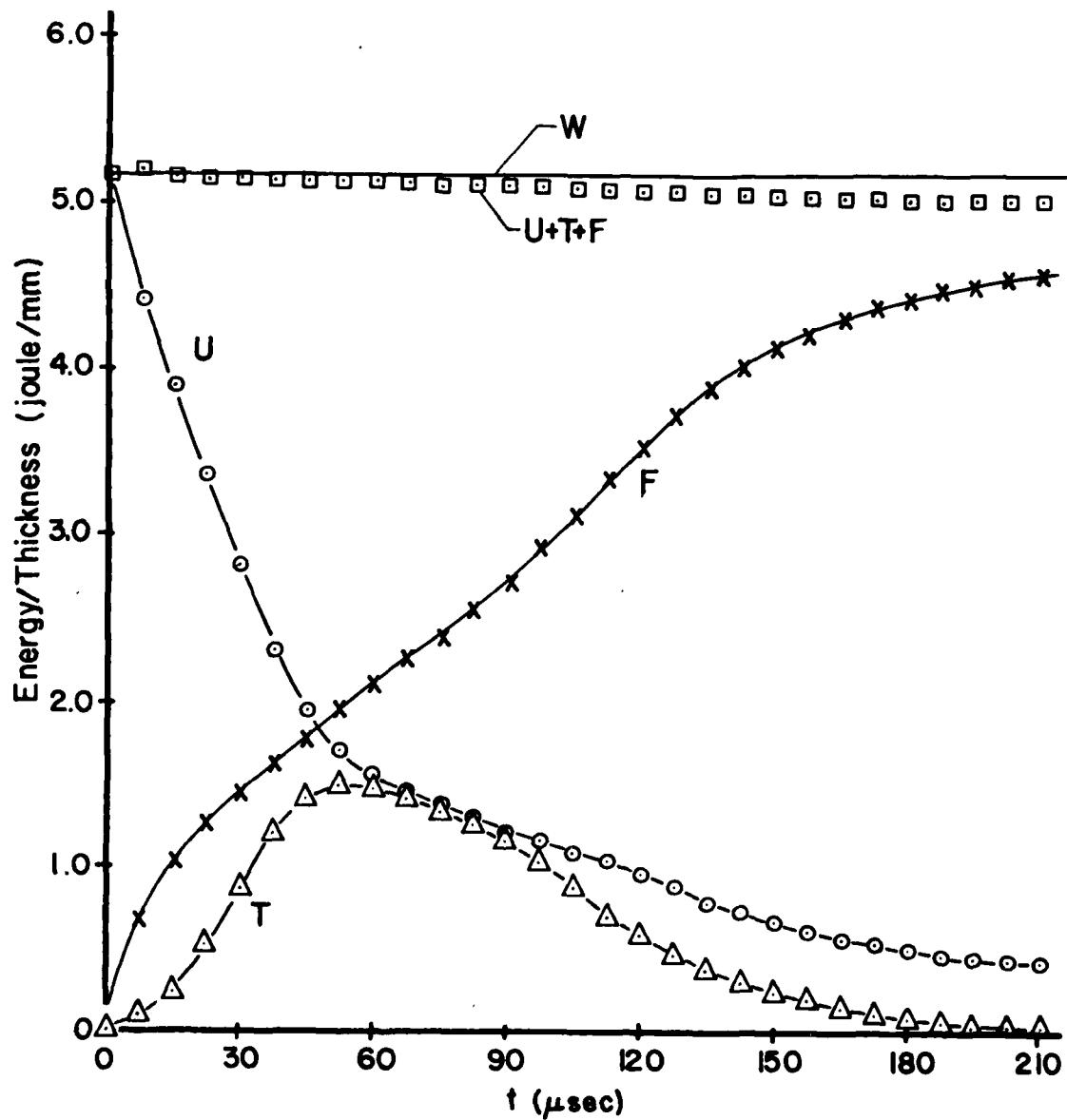
Fig. 12
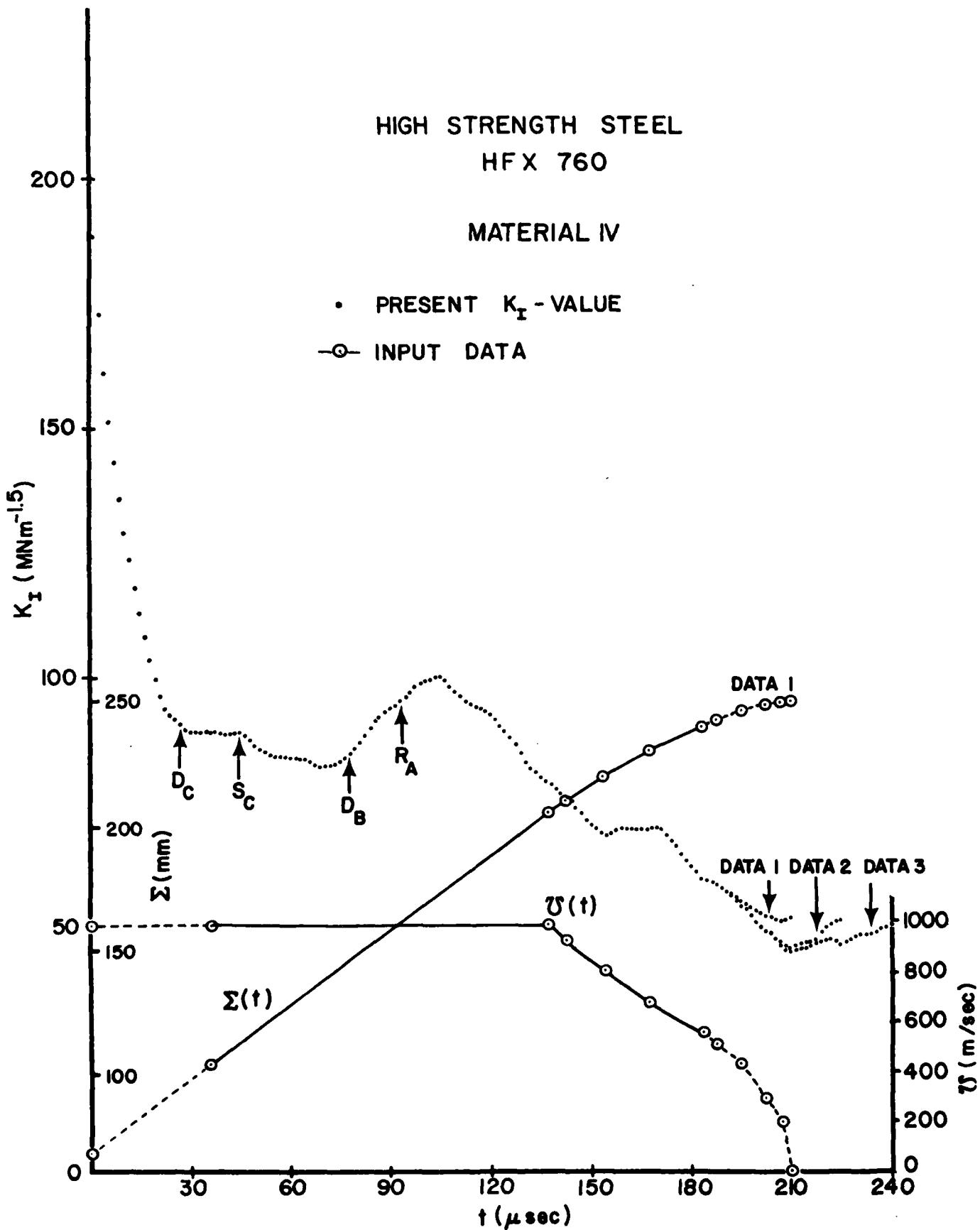
Fig. 13
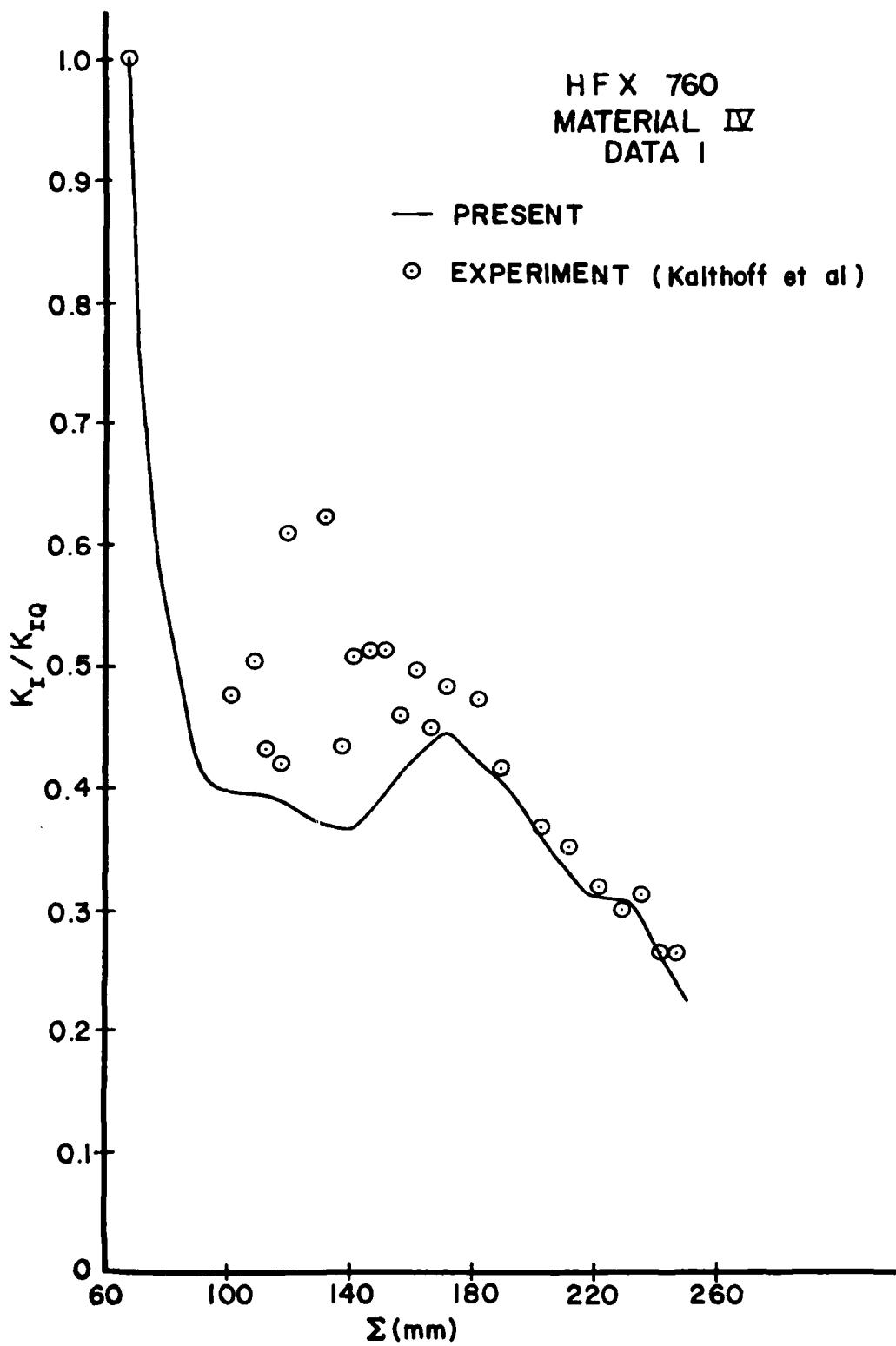
Fig. 14

HFX 760
MATERIAL IV, DATA I

Fig. 15

E = 183 GPa

ρ = 8042 Kg/m³

K_I (MNm$^{-1.5}$)

ν=0.280

ν=0.318

t(μsec)

Fig. 16

$\nu = 0.3$

$\rho = 8042 \ Kg/m^3$

$E = 183 \ GPa$

$E = 190 \ GPa$

$K_I \ (MNm^{-1.5})$

$t \ (\mu sec)$
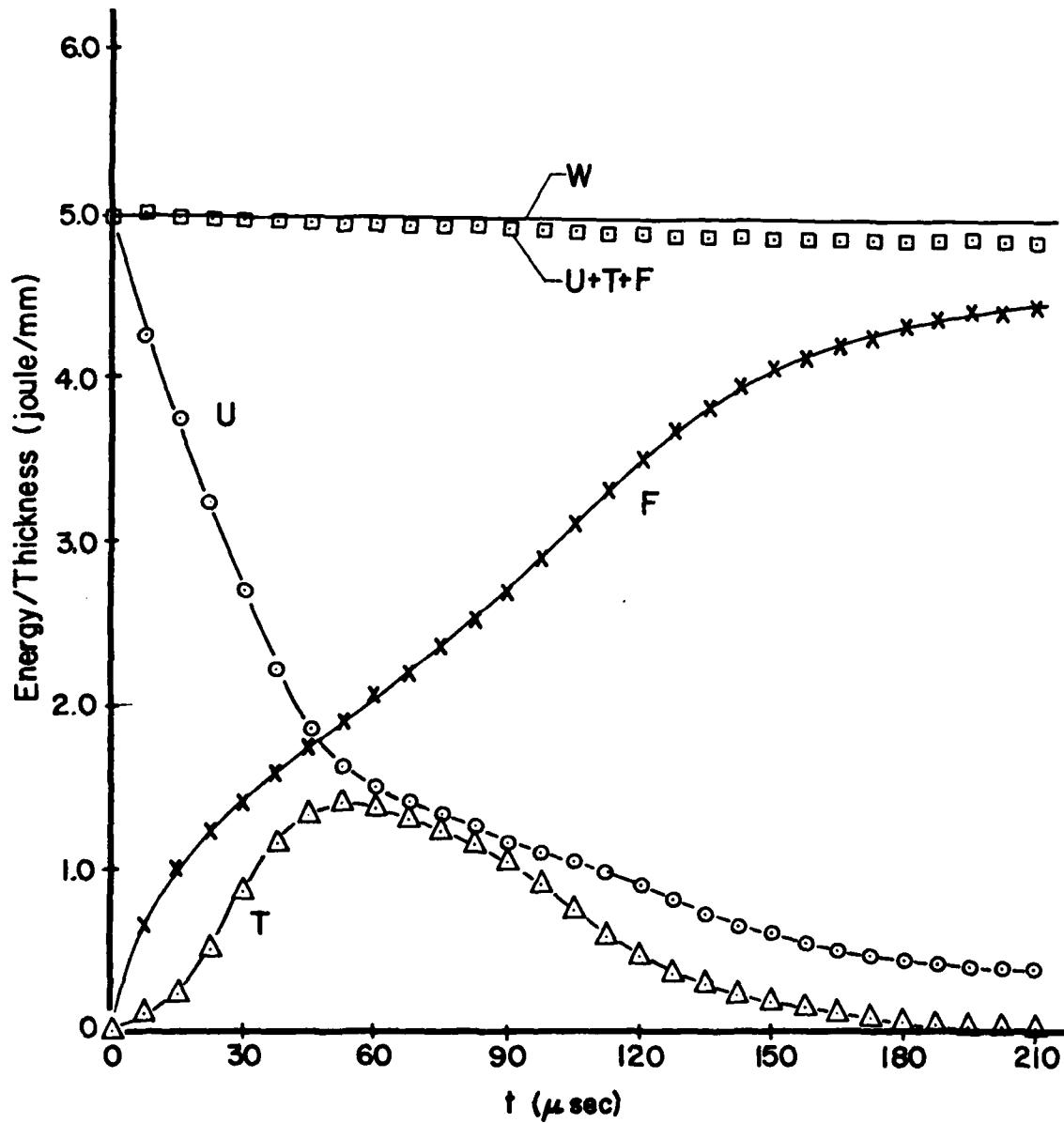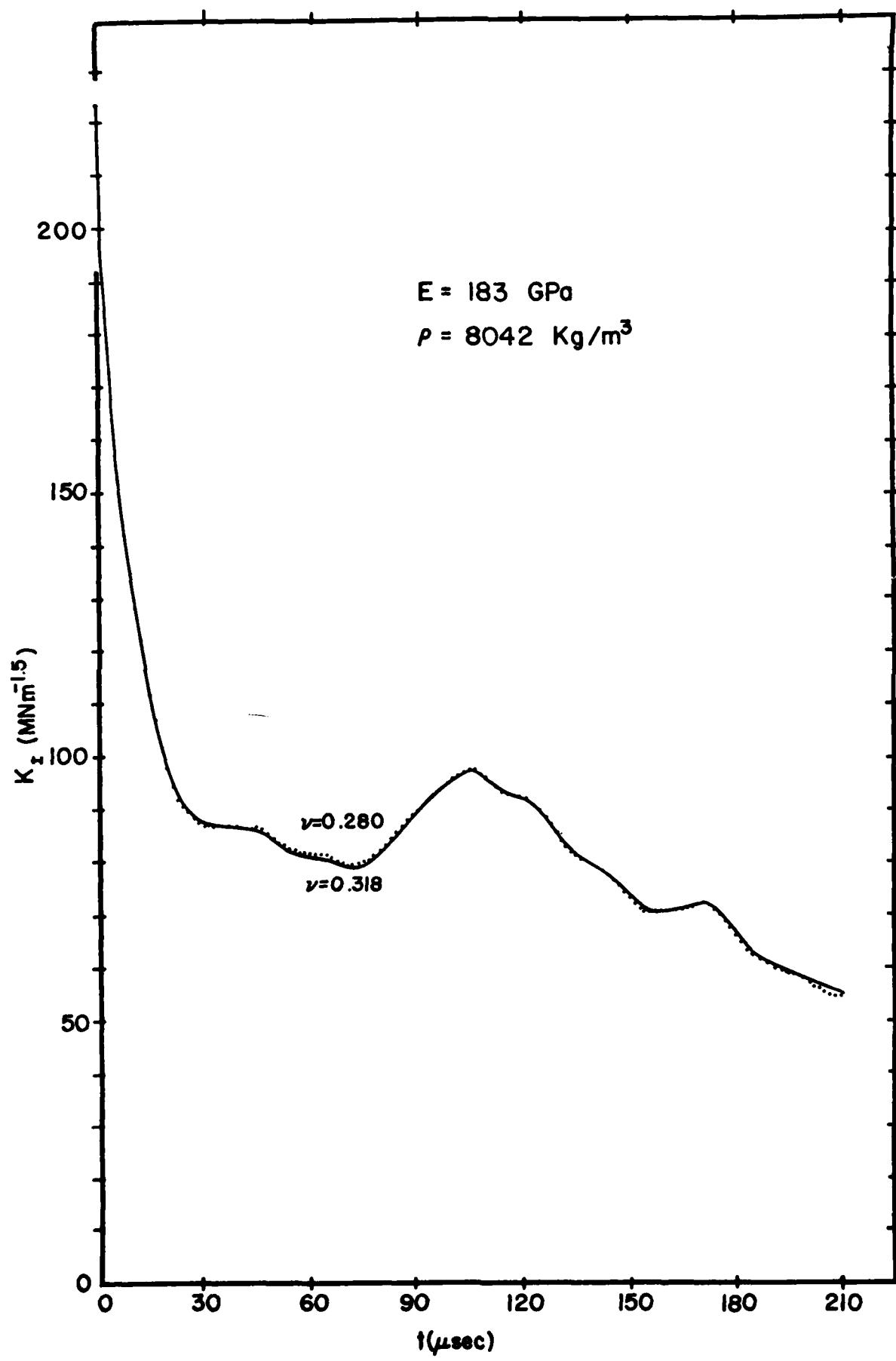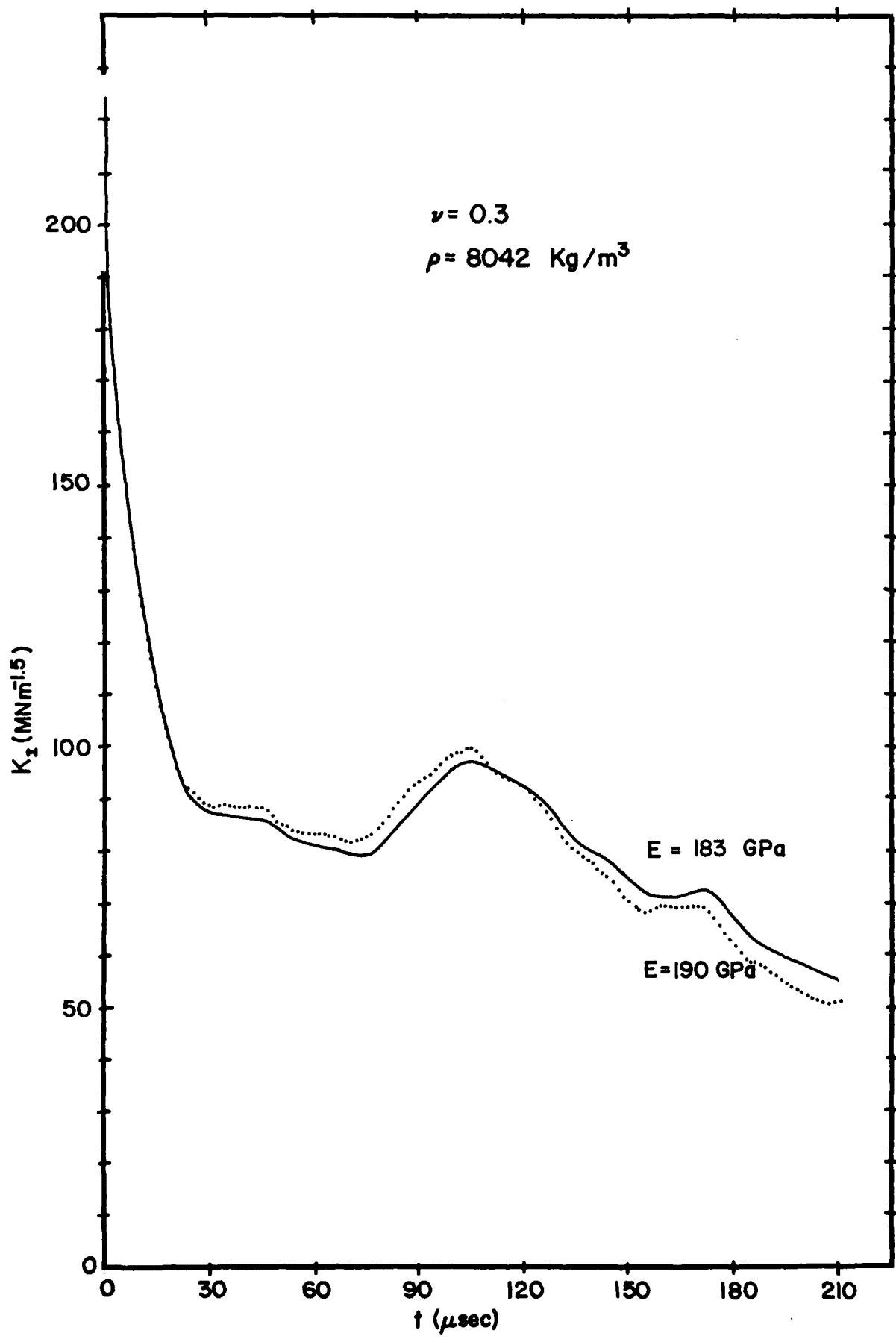
Fig. 17
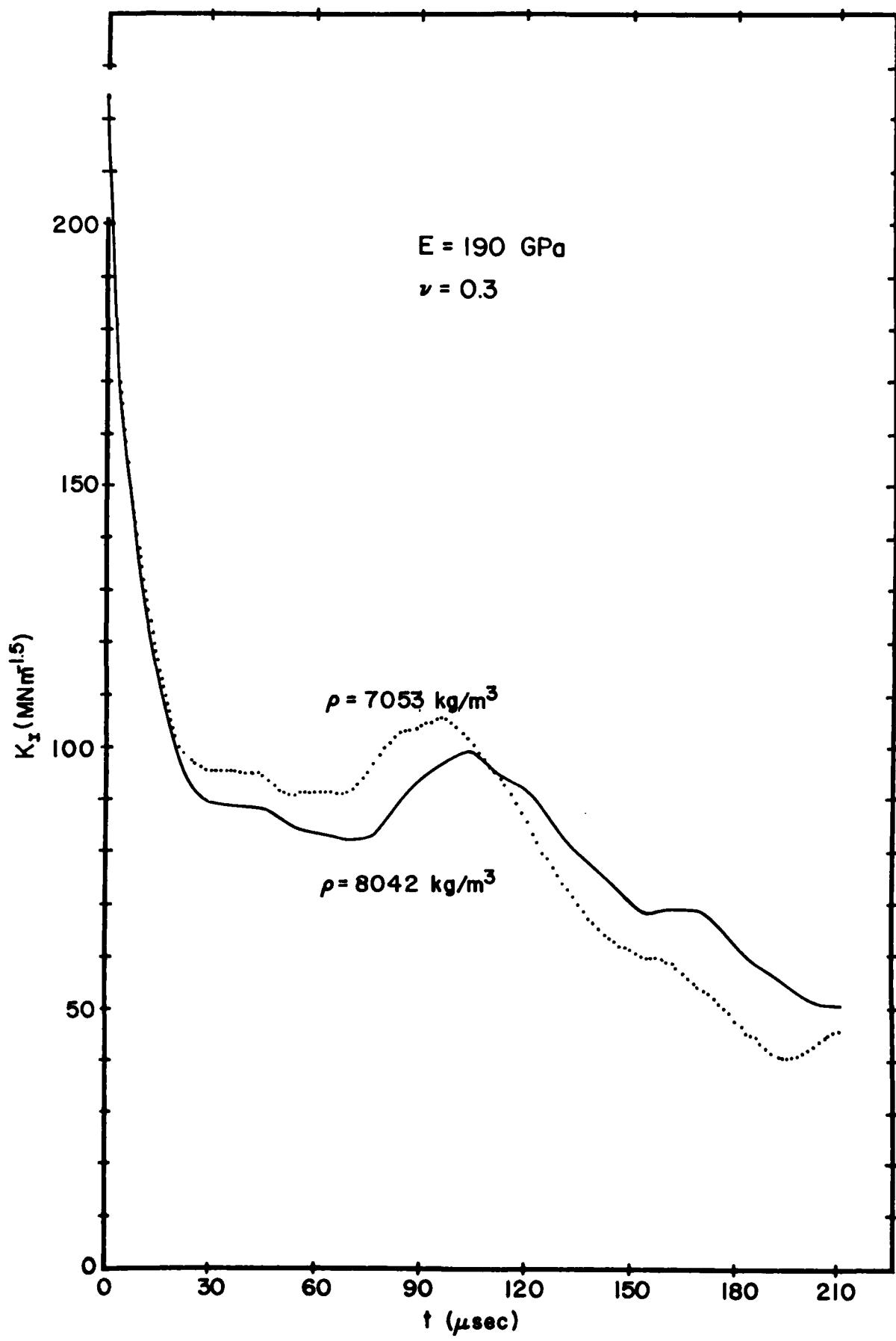
Fig. 13
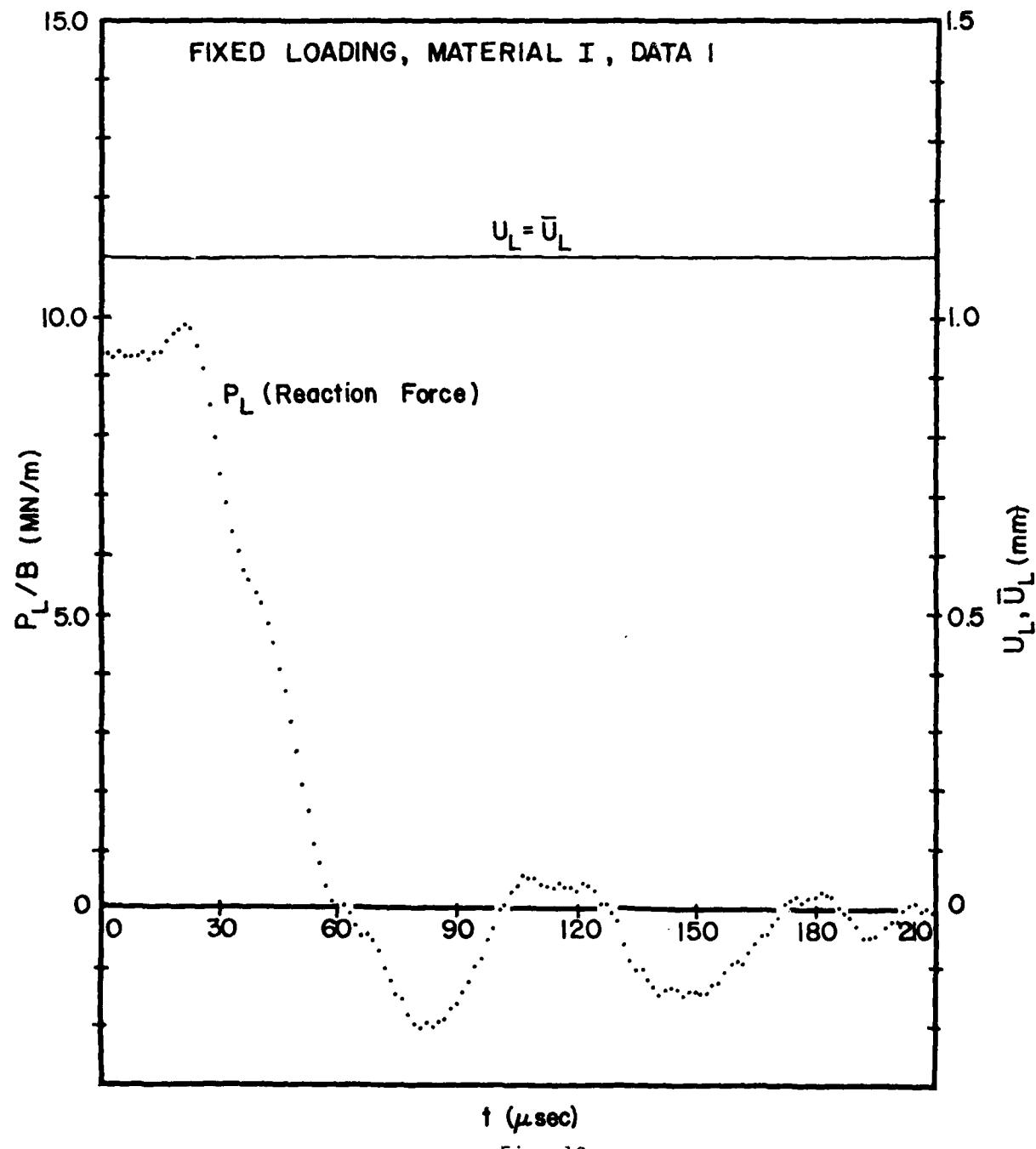
Fig. 19

FIXED LOADING, MATERIAL I, DATA I
CRACK OPENING DISPLACEMENT (y=0)

Fig. 20

WEDGE LOADING, MATERIAL I, DATA I

U_L

$\bar{U}_L$

P_L (Reaction Force)

L_I
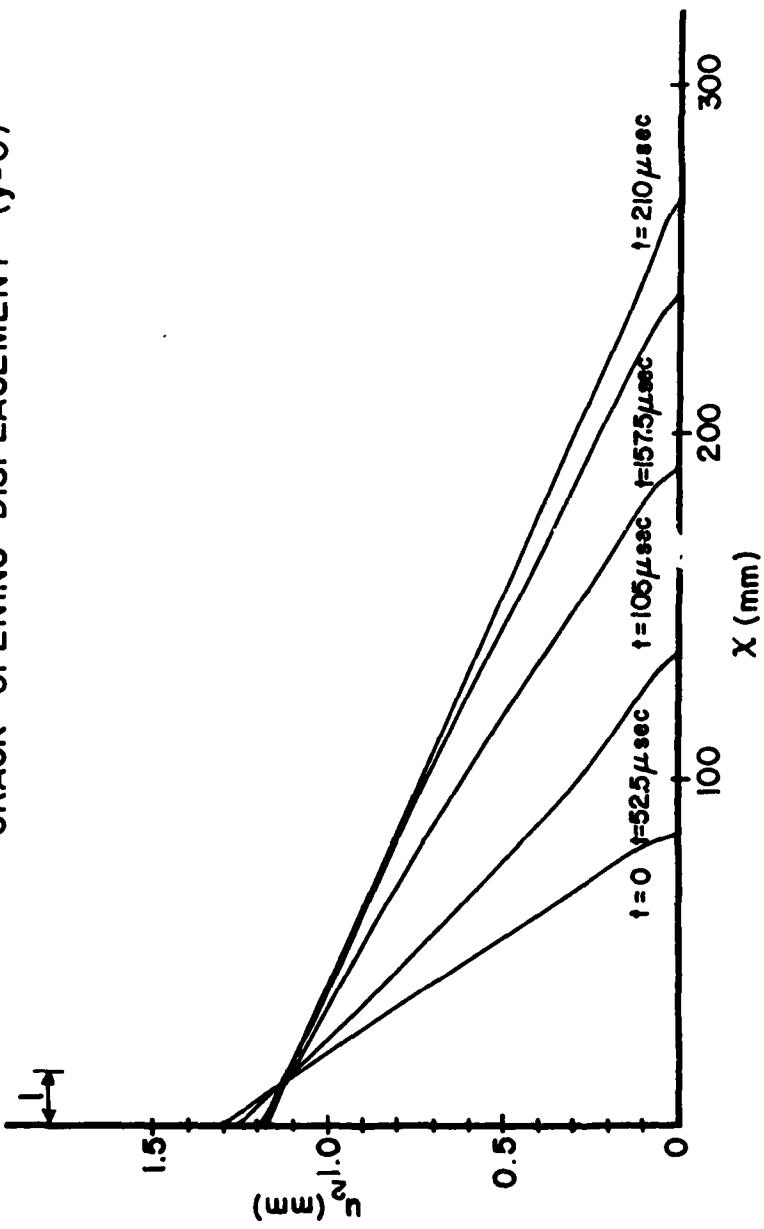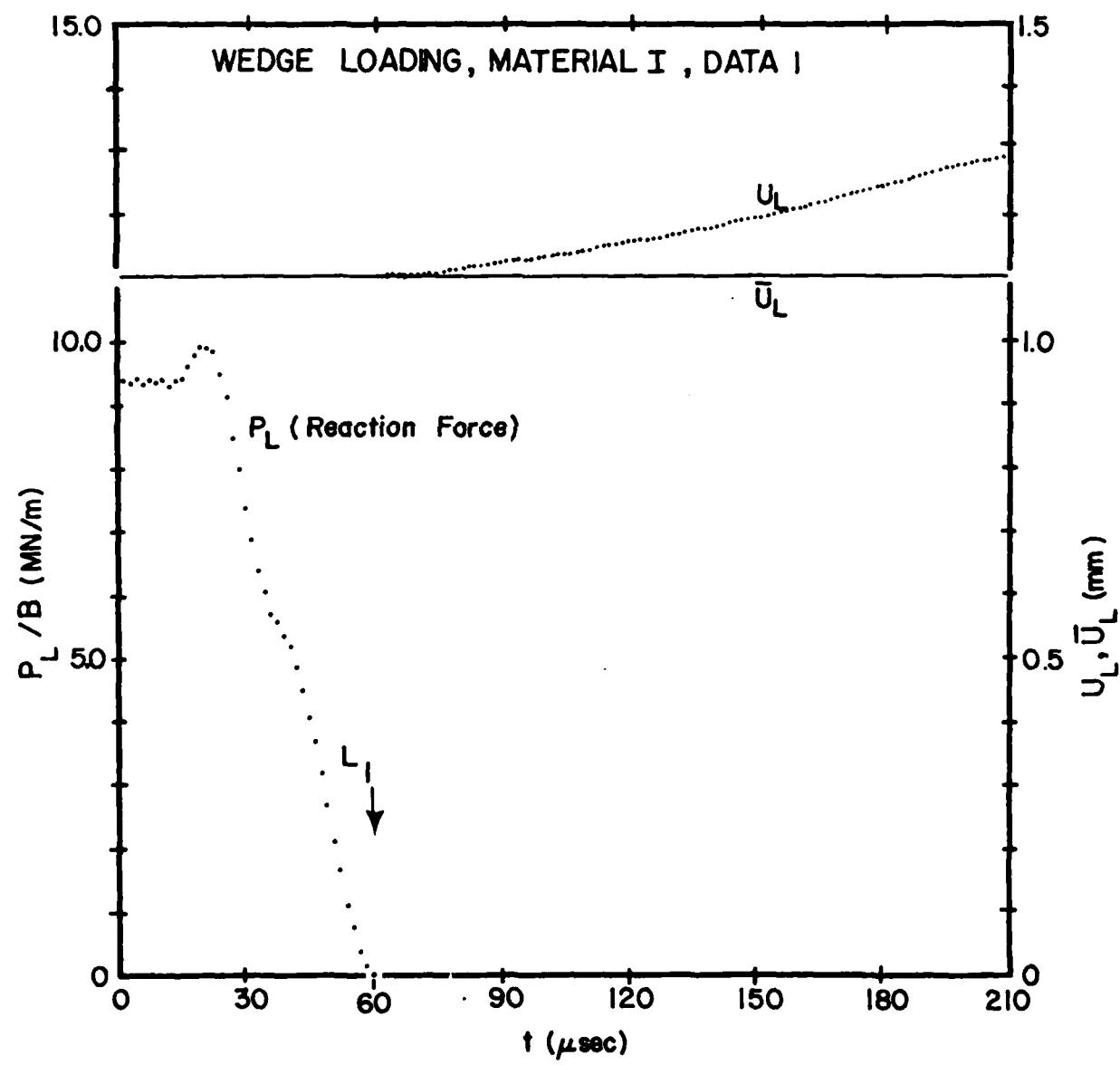
Fig. 21

WEDGE LOADING, MATERIAL I , DATA I
CRACK OPENING DISPLACEMENT
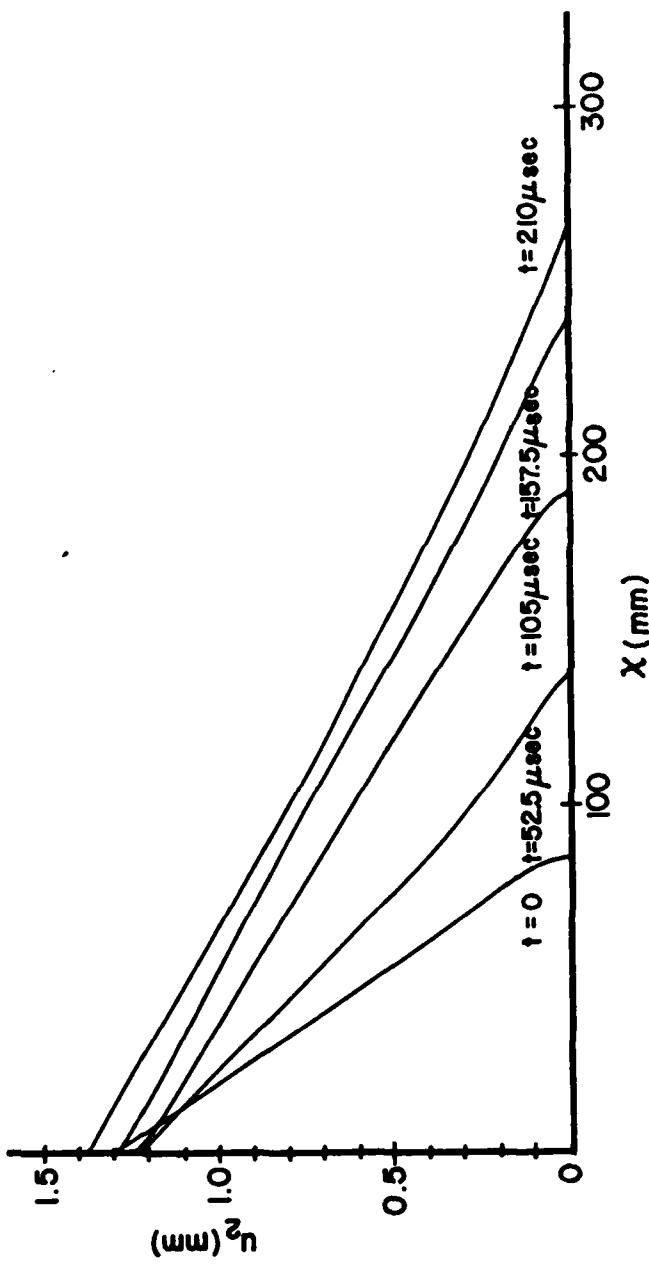
Fig. 22
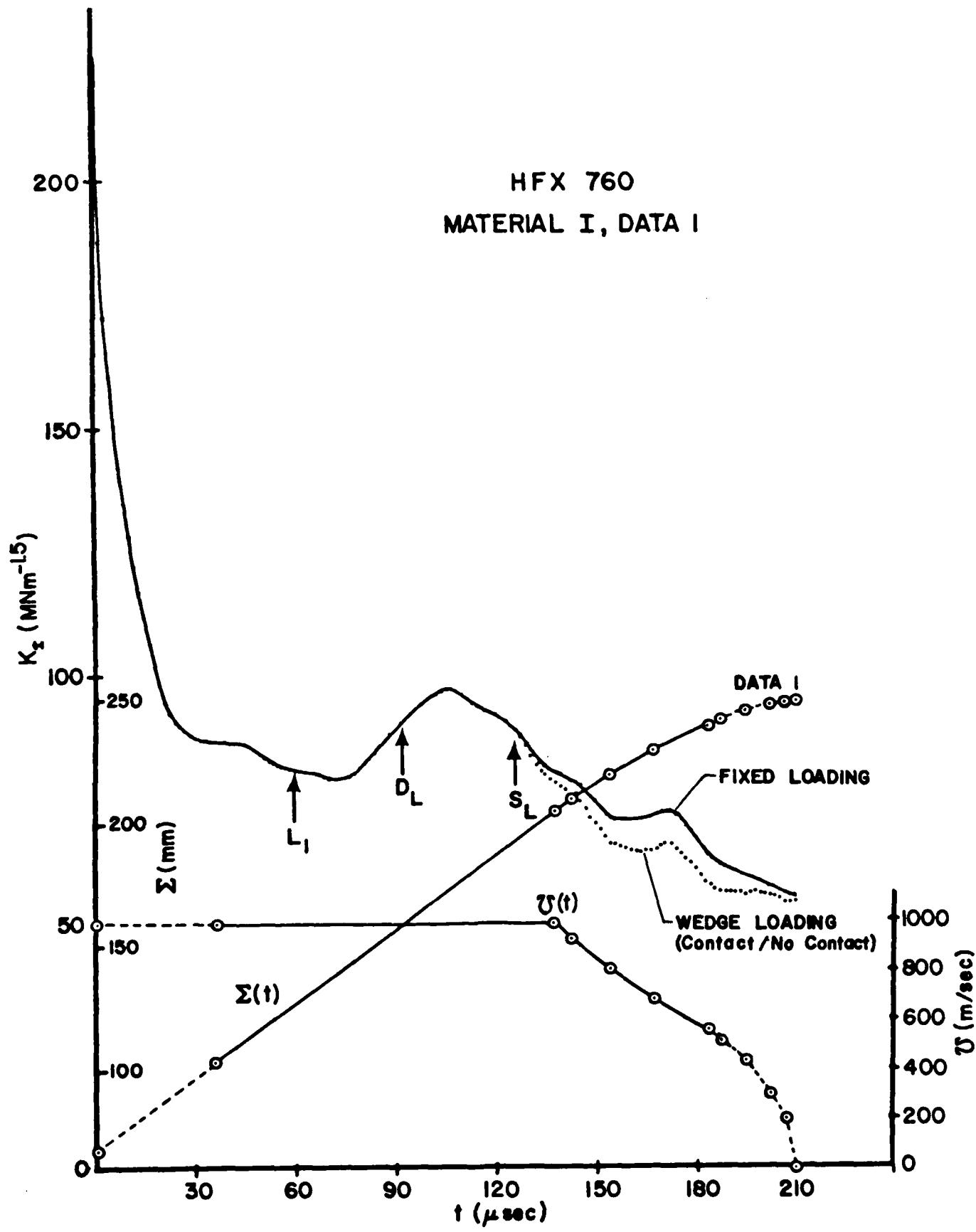
Fig. 23

WEDGE LOADING
HFX 760
MATERIAL I, DATA
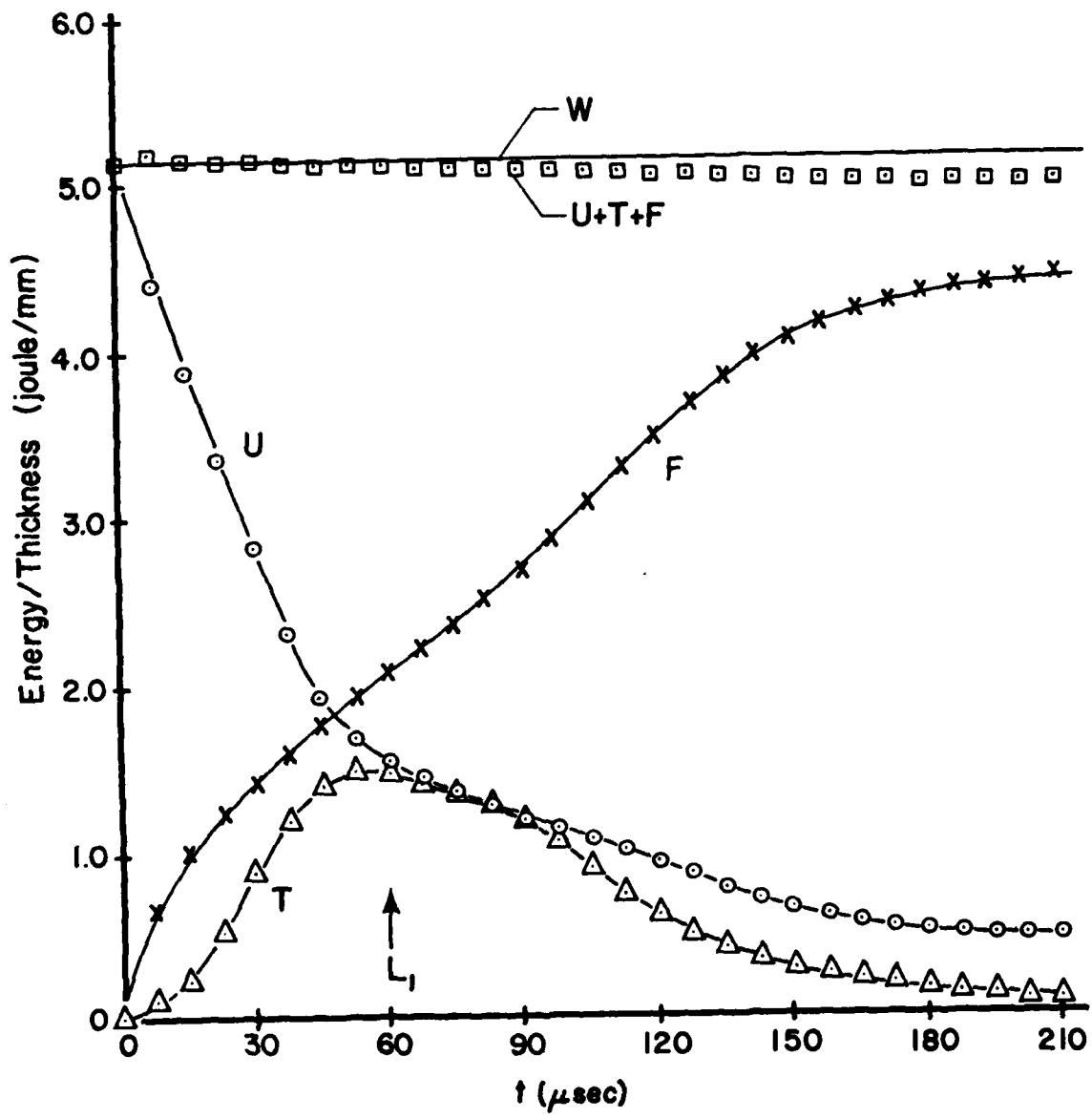
Fig. 24

REPORT DOCUMENTATION PAGE		READ INSTRUCTIONS BEFORE COMPLETING FORM
1. REPORT NUMBER 81-GIT-CACM-SNA-12	2. GOVT ACCESSION NO. AD-A103 076	3. RECIPIENT'S CATALOG NUMBER
4. TITLE *(and Subtitle)* Finite Element Simulation of Fast Fracture in Steel DCB Specimen		5. TYPE OF REPORT & PERIOD COVERED Interim Report
		6. PERFORMING ORG. REPORT NUMBER 81-GIT-CACM-SNA-12
7. AUTHOR(s) T. Nishioka, S.N. Atluri		8. CONTRACT OR GRANT NUMBER(s) N00014-78-C-0636
9. PERFORMING ORGANIZATION NAME AND ADDRESS GIT - Center for the Advancement of Computational Mechanics, School of Civil Engineering Atlanta, GA 30332		10. PROGRAM ELEMENT. PROJECT, TASK AREA & WORK UNIT NUMBERS NR064-610
11. CONTROLLING OFFICE NAME AND ADDRESS Office of Naval Research Structural Mechanics Program Dept. of Navy, Arlington, VA 22217		12. REPORT DATE July 1981
		13. NUMBER OF PAGES 43
14. MONITORING AGENCY NAME & ADDRESS*(if different from Controlling Office)*		15. SECURITY CLASS. *(of this report)* Unclassified
		15a. DECLASSIFICATION DOWNGRADING SCHEDULE

16. DISTRIBUTION STATEMENT *(of this Report)*

Unlimited

This document has been approved for public release and sale; its distribution is unlimited.

17. DISTRIBUTION STATEMENT *(of the abstract entered in Block 20, if different from Report)*

18. SUPPLEMENTARY NOTES

19. KEY WORDS *(Continue on reverse side if necessary and identify by block number)*

20. ABSTRACT *(Continue on reverse side if necessary and identify by block number)*
Results of a numerical simulation, based on an energy consistent moving singularity dynamic finite element procedure, of fast crack propagation and arrest in a high strength steel DCB specimen are presented. The influence of material properties of high strength steel on dynamic crack propagation and arrest is investigated. The influence of the loss of contact of specimen with the loading wedge is also critically examined. The present numerical results are compared with available experimental data. It is found that the present results agree well with available experimental data, and the crack arrest toughness

DD _{1 JAN 73} 1473   EDITION OF 1 NOV 65 IS OBSOLETE

values obtained in the present analysis correlate well with the ratio of the maximum kinetic energy of the specimen to the input energy.

DATE
ILMED
-8